

# Modeling temporal dependence in a sequence of spatial random partitions driven by spanning tree: an application to mosquito-borne diseases

Jessica Pavani<sup>1</sup>, Rosangela Helena Loschi<sup>2</sup> & Fernando Andrés Quintana<sup>1</sup>

<sup>1</sup>Departamento de Estadística, Pontificia Universidad Católica de Chile, Santiago, Chile

<sup>2</sup>Departamento de Estatística, Universidade Federal de Minas Gerais, Belo Horizonte, Brazil

## Abstract

Spatially constrained clustering is an important field of research, particularly when it involves changes over time. Partitioning a map is not simple since there is a vast number of possible partitions within the search space. In spatio-temporal clustering, this task becomes even more difficult, as we must consider sequences of partitions. Motivated by these challenges, we introduce a Bayesian model for time-dependent sequences of spatial random partitions by proposing a prior distribution based on product partition models that correlates partitions. Additionally, we employ random spanning trees to facilitate the exploration of the partition search space and to guarantee spatially constrained clustering. This work is motivated by a relevant applied problem: identifying spatial and temporal patterns of mosquito-borne diseases. Given the overdispersion present in this type of data, we introduce a spatio-temporal Poisson mixture model in which mean and dispersion parameters vary according to spatio-temporal covariates. The proposed model is applied to analyze the number of dengue cases reported weekly from 2018 to 2023 in the Southeast region of Brazil. We also evaluate model performance using simulated data. Overall, the proposed model has proven to be a competitive approach for analyzing the temporal evolution of spatial clustering.

**Keywords:** Bayesian spatio-temporal clustering; Correlated partitions; Dengue; Overdispersion; Product partition model.

## 1 Introduction

Growing awareness of environmental threats has led researchers to explore the spatial and temporal patterns of vector-borne diseases. In recent decades, outbreaks of these diseases have raised, reaching areas that were once unaffected. As a result, analyzing spatio-temporal clustering has become crucial for identifying regions and time periods with high incidence and for linking these patterns to environmental and social factors. We propose a new Bayesian spatio-temporal clustering model specifically designed to tackle mosquito-borne diseases. Our study aims to identify and group neighboring regions with similar infection dynamics while also investigating how these spatial patterns evolve over time.

We integrate spanning trees (Jungnickel, 2013) and product partition models (PPM, Hartigan, 1990) to address temporal dependence in spatial random partitions. This combination was initially proposed by Teixeira et al. (2015) as a mechanism to reduce the search space of spatial partitions and guarantee spatially constrained clustering. However, as illustrated by Teixeira et al. (2019), when applied to spatio-temporal data through the construction of a spatio-temporal graph, the search space can still be overwhelmingly large. Furthermore, while the spatio-temporal graph captures temporal dependence, it lacks a clear mechanism to quantify such relationship using standard time series methods. To address these shortcomings, we introduce a novel approach that generates trees from the spatial graph and allows them to evolve over time. We sample trees independently at each time point, subsequently pruning them to create partitions. Temporal dependence is incorporated into the pruning process through edge removal probabilities. These probabilities can change over time and are modeled as an autoregressive structure (Jara et al., 2013). Additionally, we

utilize Poisson mixture models to tackle the issue of overdispersion, common in this kind of data (Saraiva et al., 2022). In particular, we employ a Poisson-inverse Gaussian (PIG) model, that has proven to be more efficient than other alternatives for modeling overdispersed and heavy-tailed data (Barreto-Souza and Simas, 2015; Perrakis et al., 2015). Our formulation includes a spatio-temporal dispersion component, and it assumes that, given a positive latent variable representing heterogeneity, the response variables are independent and identically distributed (iid) Poisson realizations. Their rate is determined by a random effect that accounts for heterogeneity and a mean component that is linked to explanatory variables through a log-link function (see Section 4.1).

In summary, this study tackles the challenge of creating a prior distribution for sequences of random spatial partitions that can adapt to various spatio-temporal clustering patterns. Our aim is to uncover spatial and temporal trends in mosquito-borne diseases. Key contributions include: (i) integrating spanning trees into a hierarchical Bayesian model for a new spatio-temporal product partition model; (ii) introducing a method to incorporate temporal dependence in spatial random partitions to assess temporal autocorrelation; (iii) employing an overdispersed Poisson mixture model with parameters influenced by spatial, temporal, and spatio-temporal covariates; and (iv) identifying spatio-temporal clusters to aid policymakers in disease prevention and control strategies. The remainder of this manuscript is organized as follows: Section 2 presents a literature review of related work. Section 3 discusses the motivating data. Section 4 outlines the hierarchical model for overdispersed count data and introduces a spatio-temporal PPM driven by a spanning tree, including guidance for prior elicitation. In Section 5, we detail simulation studies that assess the model’s performance. Section 6 presents results from applying the model to mosquito-borne disease data. The paper concludes with a discussion in Section 7. Appendix is provided with computation details, simulations, and additional results.

## 2 Related works

The PPM-based clustering is a flexible strategy for modeling heterogeneous data and has been used for various purposes. The main feature of PPM is to express the prior distribution of a partition  $\pi = \{\mathcal{C}_1, \dots, \mathcal{C}_k\}$  of  $n$  areal units into  $k$  clusters in a product form such that  $\mathbb{P}[\pi = \{\mathcal{C}_1, \dots, \mathcal{C}_k\}] \propto \prod_{j=1}^k C(\mathcal{C}_j)$ , where the cohesion function  $C(\mathcal{C}_j)$  is any nonnegative function measuring how likely the elements of  $\mathcal{C}_j$  are to co-cluster. From a PPM perspective, the number of clusters is not fixed *a priori*, and its behavior is derived from the distribution of random partitions. More details will be provided later in Section 4.2, and a general review can be found in Quintana et al. (2018). In the spatial context, Hegarty and Barry (2008) introduced a prior for the random partitioning of areal data based on the number of neighbors. This strategy was later applied to the spatio-temporal context (Cremaschi et al., 2023; Pavani and Quintana, 2024). In terms of geo-referenced data, Page and Quintana (2016) developed a prior distribution that considers the distance between areas.

Although clustering strategies based on PPM have been gaining traction in the literature, the large number of possible partitions comprising the search space makes computation challenging. To facilitate the exploration of the partition space, Teixeira et al. (2015) incorporated random spanning trees into PPM for areal clustering, which also ensures that the clustering remains spatially constrained. The spanning tree is a well-established method for effective regionalization in machine learning (Assunção et al., 2006) and continues to garner interest for new advancements (Duan and Dunson, 2023; Tam et al., 2024). In clustering analysis, it reduces the search space by creating a connected subgraph that includes all nodes without cycles. This contrasts with the original PPM, which requires examining all possible partitions of the full graph; spanning trees limit partitions to those compatible with the tree, enabling contiguous clustering and the detection of irregular shapes. By pruning trees, the spatial constraints is inherently respected, ensuring connected clusters. Studies such as Teixeira et al. (2015), Luo et al. (2021), Criscuolo et al. (2023), and Luo et al. (2023) further highlight the advantages of spanning trees in spatial clustering and regression settings. Additionally, Teixeira et al. (2019) extended the strategy presented in Teixeira et al. (2015) to the spatio-temporal context by building a graph that links each region to its neighboring areas at time  $t$ , as well as to itself and its neighbors at the subsequent time  $t + 1$ . Thus, each tree takes spatial and temporal information into account. When

pruning these trees, spatio-temporal partitions are automatically obtained, with dependence inherited from the graph structure.

Other spatio-temporal clustering methods are documented in the literature. Napier et al. (2018) proposed a spatio-temporal mixture model that categorizes regions based on their temporal patterns using probabilities from a Dirichlet distribution. Similarly, Zhong et al. (2024) introduced a model that groups adjacent areas with similar disease spread using spanning trees. Both models classify temporal trends. Other studies focus on the temporal correlation of random probability measures. Gutiérrez et al. (2016), Jo et al. (2017), and De Iorio et al. (2023) integrated dependence through stick-breaking representations, and Caron et al. (2017) utilized a generalized Pólya urn scheme. Page et al. (2022) introduced a method for modeling dependence in random partition sequences, using a PPM prior combined with an auxiliary variable for partition similarity. Recently, multiview clustering approaches have emerged. Franzolini et al. (2024) applied a conditional partially exchangeable model to link clustering arrangements across features, while Dombowsky and Dunson (2024) used a nonparametric prior to create dependent random distributions centered around a random product measure. Additionally, Giampino et al. (2024) employed a state-space modeling framework to capture dependence between partitions, highlighting temporal evolution.

### 3 Motivating dataset

Brazil has the highest number of mosquito-borne disease cases in the Americas, particularly dengue fever, which the World Health Organization (WHO) has flagged as a potential global epidemic. Dengue poses serious health risks and is a leading cause of child mortality in parts of Asia and Latin America. The first dengue cases in Brazil appeared in the early 1980s in Roraima, and the disease has persisted across the nation since then. After peaking in 2023 with over three million cases, Brazil is confronting an even larger outbreak in 2024, with reported cases during the first five weeks of the year up by 378% compared to the same timeframe in 2023. Our study focuses on the Southeast region, which includes the states of Espírito Santo, Minas Gerais, Rio de Janeiro, and São Paulo, home to nearly 90 million people across 145 microregions. Cases were tracked weekly over 313 epidemiological weeks, from January 2018 to December 2023, with a total of 5,309,984 cases (see Figure 6). Additional figures can be found in the Appendix.

Analyzing data on mosquito-borne diseases like dengue is challenging, particularly due to its geographical distribution. Figure 1 illustrates the spatial distribution of standardized incidence ratios (SIR) for 2018 and 2023. For each area  $i = 1, \dots, 145$ , SIR is defined as the ratio of observed counts to expected counts, i.e.,  $SIR_i = Y_i/E_i$ , where  $E_i$  denotes the total number of cases that one would expect if the population of the  $i$ -area behaved the way the standard population behaves (Moraga, 2019, Chapter 5). It indicates whether the disease risk is lower ( $SIR < 1$ ), equal ( $SIR = 1$ ), or higher ( $SIR > 1$ ) than expected from the standard population. Dengue SIR patterns are similar in neighboring areas, forming large clusters at times, but they evolve over time and vary with seasons. For instance, during the summer of 2018, SIR was consistent across most regions with few hotspots, whereas in summer 2023, the southern zones showed significantly lower SIR than the northern ones. A comparison of winter SIR from 2018 to 2023 highlights the impact of climate change, as 2023 exhibits higher SIR levels and more clusters. This data pattern poses both practical modeling challenges for mosquito-borne diseases and theoretical challenges in developing models that account for the temporal evolution of spatial clusters.

In addition to geographic challenges, we must consider the temporal patterns of mosquito-borne diseases, which are influenced by changing weather and climate conditions. These diseases typically follow seasonal trends and exhibit yearly variations linked to meteorological factors (Franklinos et al., 2019). Temperature significantly affects the spread of vector-borne illnesses, with extreme temperatures threatening vector survival, as optimal growth occurs between 22 and 32°C (Marinho et al., 2016). Humidity also plays a crucial role, as low humidity increases mosquito desiccation risk. Therefore, we included minimum temperature and minimum humidity as spatio-temporal covariates to explain the mean and dispersion of the data (see Section 4.1 for details). Their temporal trends during the study period are shown in Figure 8, while their spatial distributions are depicted in Figures 9 and 10. From now on, for simplicity, we will refer to minimum temperature and minimum humidity as temperature and humidity, respectively. Socio-demographic factors

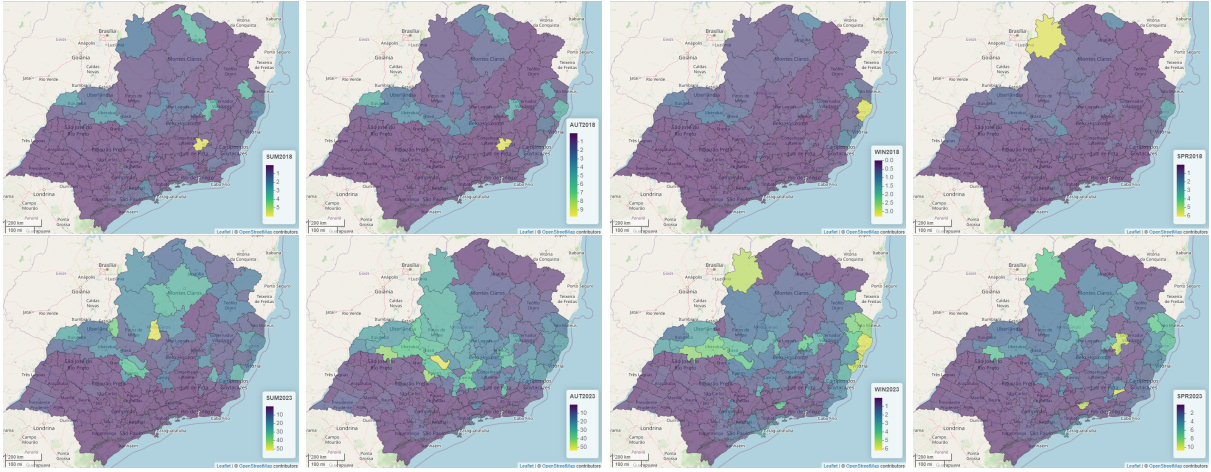


Figure 1: Spatial distribution of standardized incidence ratios of dengue across 145 microregions in the Brazilian Southeast region in 2018 (top) and 2023 (bottom), in summer (1st. column), autumn (2nd. column), winter (3rd. column), and spring (4th. column).

also influence mosquito-borne diseases, prompting us to include the Human Development Index (HDI) as a spatial variable to analyze mean case numbers. The HDI, which integrates life expectancy, education, and income, is a key indicator of human development. We retrieved HDI values from the 2010 Demographic Census for each regional unit. Figure 11 depicts the HDI's spatial distribution, revealing a distinctive pattern.

## 4 Model specification

Consider a map with  $n$  areas that remain constant over time, with  $i = 1, \dots, n$ . Our model incorporates temporal structure of the data through two time units: seasons, denoted by  $s = 1, \dots, S$ , and epidemiological weeks, denoted by  $t = 1, \dots, T$ . Seasons refer to summer, autumn, winter and spring, listed in that order, and each season lasts approximately 13 weeks. Therefore,  $T = 13 \times S$ . Cluster labels in season  $s$  are denoted by  $j_s = 1, \dots, k_s$ , where  $k_s$  is the total number of clusters in season  $s$ .

### 4.1 Modeling overdispersed count data

Denote by  $y_{it}$  the number of cases registered in area  $i$  during week  $t$  and by  $z_{is}$  the random effect accounting for heterogeneity in area  $i$  and season  $s$ . The proposed Poisson-inverse Gaussian regression model is specified as

$$(y_{it} | O_{it}, \lambda_{it}, z_{is}) \stackrel{ind}{\sim} \text{Poi}(O_{it}\lambda_{it}z_{is}), \quad 13 \times (s-1) + 1 \leq t \leq 13 \times s, \quad (1)$$

$$(z_{is} | \psi_{is}) \stackrel{ind}{\sim} \text{IG}(1, \psi_{is}), \quad (2)$$

where  $O_{it}$  and  $\lambda_{it} > 0$  respectively denote the offset and the component accounting for the mean in area  $i$  and week  $t$ , and  $\psi_{is} > 0$  is the shape parameter of the inverse-Gaussian (IG) distribution in area  $i$  and season  $s$ . The distribution in (2) imposes  $\mathbb{E}(Z_{is}) = 1$  and  $\mathbb{V}(Z_{is}) = \psi_{is}^{-1}$ . By assuming (1)-(2), the marginal distribution of the response variable is  $(y_{it} | \lambda_{it}, \psi_{is}) \stackrel{ind}{\sim} \text{PIG}(O_{it}\lambda_{it}, \psi_{is})$ , so that the marginal mean and variance are given by  $\mathbb{E}(Y_{it} | \lambda_{it}, \psi_{is}) = O_{it}\lambda_{it}$  and  $\mathbb{V}(Y_{it} | \lambda_{it}, \psi_{is}) = O_{it}\lambda_{it} + (O_{it}\lambda_{it})^2\psi_{is}^{-1}$ , respectively (Hilbe, 2014, Chapter 6). Thus, for any positive random variable  $Z_{is}$ , we obtain an overdispersed distribution, where  $\psi_{is}$  is the dispersion parameter (Barreto-Souza and Simas, 2015).

As commonly assumed, we consider a regression structure for  $\lambda_{it}$  using the log-link function. To account for seasonal effects in the mean, we consider a spatio-temporal random intercept that is specific to spatial

clusters and seasons. Let  $\theta_{is}$  be the spatio-temporal parameter for area  $i$  and season  $s$ . To define the random clustering structure on  $\theta_{is}$  at each season  $s$ , we consider a graph  $\mathcal{G}$  of neighboring areas. Let  $\boldsymbol{\pi}_s = \{\mathcal{C}_1^s, \dots, \mathcal{C}_{k_s}^s\}$  be a random partition in season  $s$  obtained by removing some specific edges in  $\mathcal{G}$  (see Section 4.2 for a discussion). Given  $\boldsymbol{\pi}_s$ , we assume that the parameters  $\theta_{is}$  are identical across all areas within each cluster, that is,  $\theta_{is} = \theta_{j_s s}^*$  for all  $i \in \mathcal{C}_{j_s}^s$ , where  $\theta_{j_s s}^*$  is the cluster-season-specific parameter for all areas belonging to cluster  $\mathcal{C}_{j_s}^s$ . Thus,  $\lambda_{it}$  is given by

$$\lambda_{it} = \exp\{\mathbf{X}_{it}^\top \boldsymbol{\beta}\} \theta_{j_s s}^*, \quad i \in \mathcal{C}_{j_s}^s, \quad (3)$$

$$\boldsymbol{\beta} \sim N_{p_1}(\boldsymbol{\mu}_\beta, \boldsymbol{\Sigma}_\beta), \quad (4)$$

where  $\mathbf{X}_{it}$  is a  $p_1$ -dimensional design vector that considers spatio-temporal predictors for area  $i$  at week  $t$  and  $\boldsymbol{\beta} = \{\beta_1, \dots, \beta_{p_1}\}$  denotes their respective coefficients. We assume that

$$\theta_{j_s s}^* \stackrel{iid}{\sim} \text{Ga}(a_\theta, b_\theta), \quad a_\theta > 0, \quad b_\theta > 0. \quad (5)$$

As the vector  $\boldsymbol{\beta}$  does not include a term for the intercept,  $\log(\theta_{j_s s}^*)$  works as the random intercept for cluster  $j_s$  in season  $s$ . Thus, all areas belonging to the same spatial cluster share the same value for  $\theta$  during all weeks of a season. This assumption is driven by the specific characteristics of mosquito-borne diseases. Figure 6 shows that there is little variation in the number of cases reported from one week to the next, indicating that clustering is unlikely to change on a weekly basis. However, there is a clear seasonal pattern, with an increase in the number of cases occurring between October of one year and May of the following year. Figure 7 also supports the notion that spatial clustering behavior is seasonal. By incorporating a cluster-season-specific intercept in the model, we account for the overall impact on the Poisson distribution rate. We also allow for individual behavior in each area during each season. Areas are grouped together in each season based on the similarity of the  $\theta_i$ 's. Different groupings for each season are assumed to follow the structure detailed in Section 4.2.

Although the dispersion parameter in (2) is usually assumed to be constant, it may be more reasonable to allow it to vary over time and space. Following Barreto-Souza and Simas (2015), we consider a log-linear structure for  $\psi_{is}$  letting

$$\psi_{is} = \exp\{\mathbf{V}_{is}^\top \boldsymbol{\delta}\}, \quad (6)$$

where  $\mathbf{V}_{is}$  is a  $p_2$ -dimensional design vector considering spatio-temporal predictors that might affect the dispersion, and  $\boldsymbol{\delta} = \{\delta_0, \dots, \delta_{p_2}\}$  represents their effects. We also assume

$$\boldsymbol{\delta} \sim N_{p_2}(\boldsymbol{\mu}_\delta, \boldsymbol{\Sigma}_\delta). \quad (7)$$

Unlike the mean, which is assumed to be different for each area  $i$  and week  $t$ , dispersion is area-specific but remains constant within each season  $s$ . This assumption is justified by the characteristics of the context that motivates this study. The heterogeneity of mosquito-borne diseases is greater in summer than in winter (see Figure 7). This occurs because the climatic characteristics of summer are more favorable for the reproduction and spread of mosquitoes, affecting regions differently. The regression structures for both mean and dispersion can be easily modified to accommodate spatial, temporal, and/or spatio-temporal covariates, depending on the context in which the model is applied. For mosquito-borne disease data, the design matrix  $\mathbf{X}$  comprises covariates measured by area and week, while the design matrix  $\mathbf{V}$  contains information measured by area and season.

To complete the model specification, we need to specify hyperparameters for the prior distributions of the regression coefficients  $\boldsymbol{\beta}$  and  $\boldsymbol{\delta}$ , as well as for the cluster-specific parameters  $\theta_{j_s s}^*$ . Although the use of vague prior distributions is usually preferred for making posterior inferences when dealing with complex models, it is convenient to use informative priors, at least for some parameters. We consider vague priors for  $\boldsymbol{\beta}$  and  $\boldsymbol{\delta}$  by assigning them normal distributions with a mean of zero and a large variance. However, the prior distribution for the cluster-specific parameters requires more attention. As defined in (3),  $\log(\theta_{j_s s}^*)$  works as a random spatio-temporal cluster-specific intercept. Therefore, its hyperparameters should be specified according to

the expected relative risk of the disease. One way to define these values would be to consider the simplest case of the model, where data overdispersion is not observed and the covariates have no effect, i.e.,  $\mathbf{z} = \mathbf{1}$  and  $\boldsymbol{\beta} = \mathbf{0}$ . In this case,  $\theta_{is}$  is the only random effect explaining the outcome in area  $i$  and season  $s$ . When  $\boldsymbol{\theta} = \mathbf{1}$ , the outcome is entirely determined by the offset. Given this, it seems natural to set both the prior mean and variance of  $\theta_{is}$  equal to one.

## 4.2 Spatio-temporal PPM driven by spanning tree

One of our key contributions is developing a model for the temporal evolution of spatial partitions formed by contiguous clusters. Considering the seasonal impact of climate on mosquito-borne diseases, it is reasonable to expect greater fluctuations in case numbers during certain times of the year, especially when conditions favor the spread of these diseases, leading to an increase in clusters. Inspired by the approach of Teixeira et al. (2015), we propose a spatio-temporal model using spanning trees and a product partition prior for random partitions. For a deeper understanding of spanning trees, please refer to Section B of the Appendix. Our model expands on the original framework by integrating the changes in partitions over time. To account for this time evolution on the partitions, we consider that the probabilities of removing edges may vary over seasons.

As our map is constant over time, the neighborhood structure is represented by a graph  $\mathcal{G}$  that is common to all seasons. To simplify the sampling process of the posterior distribution of  $\boldsymbol{\pi}_s$ , we introduce a minimum spanning tree  $\mathcal{T}_s$  that is randomly generated from  $\mathcal{G}$  for each season  $s$ . The edges are conditionally independent and randomly removed from  $\mathcal{T}_s$  with a probability of  $\rho_s \in [0, 1]$ . Thus, a spatial partition of the areas in season  $s$  is generated. The probability  $\rho_s$  is common to all edges linking spatial vertices in season  $s$  and influences the estimated number of clusters. Large values of  $\rho_s$  induce a high expected number of clusters, while the opposite holds for small  $\rho_s$ . The cohesion function of cluster  $\mathcal{C}_{j_s}^s$  is formulated as

$$C(\mathcal{C}_{j_s}^s) = \begin{cases} \rho_s(1 - \rho_s)^{|e_{j_s}|}, & \text{if } j_s < k_s, \\ (1 - \rho_s)^{|e_{j_s}|}, & \text{if } j_s = k_s, \end{cases}$$

where  $|e_{j_s}|$  is the total number of edges not removed in  $\mathcal{C}_{j_s}^s$ , and  $k_s$  is the number of clusters in season  $s$ . Assuming this function, the prior probability of partition given the tree is

$$\mathbb{P}[\boldsymbol{\pi}_s = \{\mathcal{C}_1^s, \dots, \mathcal{C}_{k_s}^s\} \mid \mathcal{T}_s, \rho_s] = \begin{cases} \rho_s^{k_s-1}(1 - \rho_s)^{n-k_s}, & \text{if } \boldsymbol{\pi}_s \prec \mathcal{T}_s, \\ 0, & \text{otherwise.} \end{cases} \quad (8)$$

In (8),  $\boldsymbol{\pi}_s \prec \mathcal{T}_s$  denotes that partition and tree are compatible, i.e.,  $\boldsymbol{\pi}_s$  can be obtained by pruning  $k_s - 1$  edges from  $\mathcal{T}_s$ . Note that this effectively reduces the collection of partitions we consider in each season to those compatible with the corresponding tree.

Like partitions, trees also vary across seasons. To ensure compatibility between trees and partitions, we assume independence of trees over seasons. Then, we assume independent uniform distributions so that for each season  $s$ , all possible trees of  $\mathcal{G}$  are equally probable, that is,

$$\mathbb{P}[\{\mathcal{T}\}_s] = \prod_{s=1}^S \mathbb{P}[\mathcal{T}_s], \quad \mathbb{P}[\mathcal{T}_s] \propto 1. \quad (9)$$

While straightforward, the previous approach has the disadvantage of creating an independent sequence of partitions. To alleviate this problem while still keeping tractability, we consider an indirect correlation between partitions, by introducing a time-dependent structure in the vector  $\boldsymbol{\rho} = (\rho_1, \dots, \rho_S)$ . Specifically, we model  $\boldsymbol{\rho}$  with an autoregressive time series model that is constrained to the unit interval. To achieve this, we adopt the hierarchical framework introduced by Jara et al. (2013), where a sequence of beta random variables is linked through a set of exchangeable latent indicators built in an autoregressive way. For this purpose, let  $\{u_s\}$  and  $\{c_s\}$  be sequences of non-negative integer-valued latent variables. The prior distribution for  $\rho_s$ ,

given  $\{u_s\}$  and  $\{c_s\}$ , is given by

$$(\rho_s \mid u_s, \dots, u_{s-q}, c_s, \dots, c_{s-q}, v, \kappa) \stackrel{iid}{\sim} \text{Be} \left( v + \sum_{l=0}^q u_{s-l}, \kappa + \sum_{l=0}^q (c_{s-l} - u_{s-l}) \right), \quad (10)$$

$$(u_s \mid c_s, w) \stackrel{iid}{\sim} \text{Bin}(c_s, w), \quad (11)$$

$$(c_s \mid \zeta) \stackrel{iid}{\sim} \text{Poi}(\zeta), \quad (12)$$

$$(w \mid v, \kappa) \sim \text{Be}(v, \kappa), \quad (13)$$

with  $v > 0$ ,  $\kappa > 0$ , and  $\zeta > 0$ . Latent variables  $u_s$  and  $c_s$  are defined to be zero for  $s \leq 0$ . In this formulation, the role of  $\{u_s\}$  is to establish a link between the  $\rho_s$ 's. The hyperparameter  $w$  is the common success probability that determines the overall series level, and  $q \geq 1$  represents the order of the autoregressive process.

The advantages of using this approach are numerous. By defining the temporal dependence through a sequence of latent variables instead of directly on the original probability vector, we ensure a beta marginal distribution for  $\rho_s$ , specifically  $\rho_s \sim \text{Be}(v, \kappa)$  (Jara et al., 2013). This property is helpful for obtaining marginal distributions for partitions and the number of clusters in each season (Teixeira et al., 2015, 2019). By identifying how the number of clusters is distributed *a priori*, we can calculate its mean and variance as

$$\mathbb{E}(k_s \mid \cdot) = (n-1) \frac{v}{v+\kappa} + 1 \quad \text{and} \quad \mathbb{V}(k_s \mid \cdot) = (n-1) \frac{v\kappa(v+\kappa+n-1)}{(v+\kappa)^2(v+\kappa+1)}, \quad (14)$$

respectively. This is a valuable result for prior elicitation purposes, since it is clear from (14), that  $\rho_s$  directly impacts the number of clusters through its hyperparameters. If  $v = \kappa$ , the average marginal probability of removing the edge is 50%, implying an expected number of clusters around  $n/2$ . If  $v \rightarrow 0$  and/or  $\kappa \rightarrow \infty$ , then  $\{\rho_s\} \rightarrow 0$  and all areas are grouped into the same cluster. Conversely, if  $v \rightarrow \infty$  and/or  $\kappa \rightarrow 0$ , then  $\{\rho_s\} \rightarrow 1$  creating  $n$  clusters.

Another advantage of this approach lies in the temporal autocorrelation of  $\{\rho_s\}$  and consequently of  $\{\pi_s\}$ . The proposed model assumes: (i) trees are independent for each season; (ii) given the tree and the probability of removing edges, partitions are independent for each season; and (iii) probabilities of removing edges are autocorrelated over time. Thus, partitions exhibit autocorrelation due to the underlying process that drives them, something similar to the construction established in Hidden Markov Models. Within seasons, the correlation between observations occurs indirectly since they share the common parameters  $\theta$  and  $\mathbf{z}$  (see Section B.3 in the Appendix). For model (10)–(13), Jara et al. (2013) showed that the autocorrelation function of  $\{\rho_s\}$  can be computed in closed form as

$$\text{corr}(\rho_s, \rho_{s+l}) = \frac{(v+\kappa) \sum_{h=0}^{q-l} c_{s-h} + \left( \sum_{h=0}^q c_{s-h} \right) \left( \sum_{h=0}^q c_{s+l-h} \right)}{\left( v+\kappa + \sum_{h=0}^q c_{s-h} \right) \left( v+\kappa + \sum_{h=0}^q c_{s+l-h} \right)}, \quad (15)$$

for  $s, l \geq 1$ . By varying the values of  $v$ ,  $\kappa$ , and  $\{c_s\}$ , we can obtain different degrees of autocorrelation. For all  $s, l$ , and  $\mathbf{c}$ , if  $(v+\kappa) \rightarrow 0$ , then  $\text{corr}(\rho_s, \rho_{s+l}) \rightarrow 1$ , whereas, if  $(v+\kappa) \rightarrow \infty$ , then  $\text{corr}(\rho_s, \rho_{s+l}) \rightarrow 0$ . Regarding  $\mathbf{c}$ , the first term of the numerator in (15) considers shared values of  $\{c_s\}$ , while the other terms consider sets of  $\{c_s\}$  that define  $\rho_s$  and  $\rho_{s+l}$ . Hence, when  $\rho_s$  and  $\rho_{s+l}$  do not share any  $\{c_s\}$ , then  $\sum_{h=0}^{q-l} c_{s-h} = 0$ , and the autocorrelation function is driven by the values of  $v$  and  $\kappa$ . Furthermore, when  $\{c_s\} \rightarrow 0$ , then  $\text{corr}(\rho_s, \rho_{s+l}) \rightarrow 0$  for all  $s, l, v$ , and  $\kappa$ .

The full Bayesian hierarchical structure is achieved by assuming prior distributions for the remaining hyperparameters, which we choose as

$$v \sim \text{Ga}(a_v, b_v), \quad \kappa \sim \text{Ga}(a_\kappa, b_\kappa), \quad \zeta \sim \text{Ga}(a_\zeta, b_\zeta). \quad (16)$$

The choice of values for  $a_v$ ,  $b_v$ ,  $a_\kappa$ , and  $b_\kappa$  in (16) must be guided by the expected number of clusters in the first season, while the values for  $a_\zeta$  and  $b_\zeta$  impact the autocorrelation function. See Sections B.2, B.3, and D in the Appendix for further details.

Figure 2 provides a graphical representation of our proposed model, highlighting the fact that the time dependence of probabilities  $\rho$  is induced by the sequences of latent variables  $\{u_s\}$  and  $\{c_s\}$ . Even more importantly, the time dependence of the sequence of partitions  $\{\pi_s\}$  is induced by the time dependence of  $\rho$ .

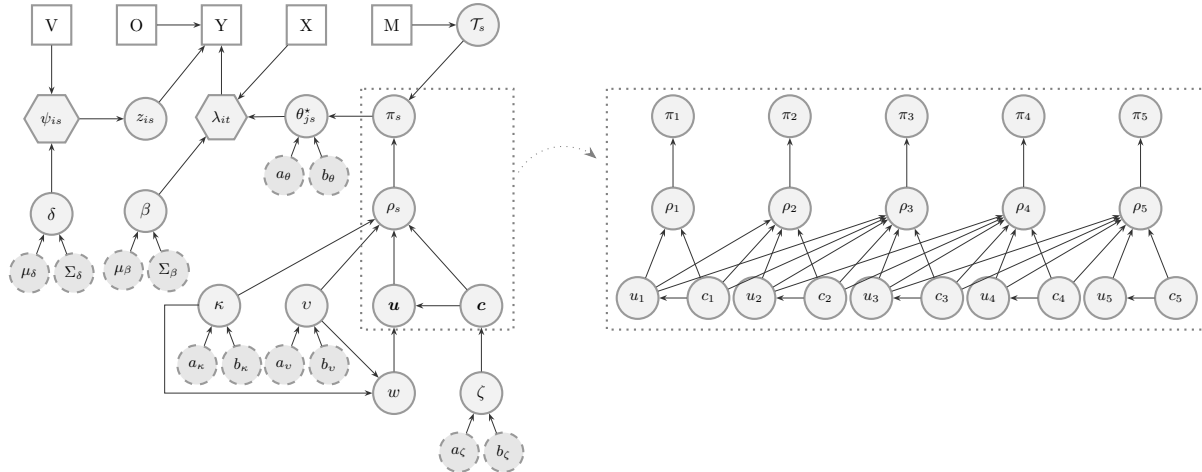


Figure 2: Graphical representation of the model highlighting an autoregressive process of order  $q = 2$ . Square nodes represent inputs –  $M$ : adjacency matrix,  $X$  and  $V$ : design matrices,  $O$ : offset, and  $Y$ : outcome. Hexagon nodes represent generated quantities. Circle nodes represent unknown (solid lines) and known (dashed lines) parameters.

## 5 Simulation study

Our goals in this section are: (i) to compare Poisson and PIG models performances in overdispersed and equidispersed spatio-temporal scenarios, and (ii) to evaluate the impact of the order of temporal dependence on clustering. In both studies, we generated 100 synthetic datasets employing the model defined in Section 4.1 for each configuration as detailed in the Appendix (Sections F.1 and F.2). To create realistic scenarios, we used the 70 microregions of Minas Gerais, Brazil, where two regions are considered neighbors if they share a geographic boundary. Furthermore, we used observed data as offset and covariates. Population size (per 100,000 people) served as the offset, while temperature and humidity were included as covariates, forming  $\mathbf{X}$  and  $\mathbf{V}$  (data details are in Section 3). Unlike  $\mathbf{X}$ , which contains weekly measurements,  $\mathbf{V}$  consists of average values for each season and includes a column of 1's for the intercept. These settings applied to all simulated datasets, with specific study details in Section F of the Appendix. After data generation, we implemented the MCMC algorithm (described in Section E of the Appendix), saving 1,000 samples from 10,000 iterations while discarding the first 70% as burn-in and thinning by 3 to reduce correlation. Convergence was monitored graphically. Prior specifications are detailed in Section F. We used the Watanabe-Akaike information criterion (WAIC, Gelman et al., 2014) to evaluate model fit and the `salsol` R package (Dahl et al., 2020) along with the variation information (VI) loss function for estimating partitions. We then calculated the Rand Index (RI, Hubert and Arabie, 1985) to assess the similarity between true and estimated partitions. Key characteristics and results for each study are summarized below, with further details in Section F.

**Simulation 1 - Comparing PIG and Poisson models when fitting equidispersed and overdispersed data** All figures and tables mentioned below can be found in Section F.1 of the Appendix. In



short, the difference in producing equidispersed and overdispersed data lies in the way the component  $z_{is}$  accounting for data heterogeneity is defined. To produce equidispersed data, it is sufficient to assume  $\mathbf{z} = \mathbf{1}$ ; thus, the mean and variance will be equal. In the other case,  $z_{is}$  is randomly generated from the IG density as presented in (2). We first evaluated the models' ability to recover regression coefficients (Table 2). The coverage associated with  $\beta$  was similar for all models. This result was expected, as the regression structure used to explain the average is the same for all datasets. In the case of  $\delta$  coefficients, we observed that when the PIG model was applied to overdispersed data, it was able to recover these parameters. However, when we fitted the PIG model to data where the mean and variance are equal, the model tended to overestimate these coefficients, especially the intercept. This occurs because, when estimating high values for  $\delta$ , we obtain high values for  $\psi$ , which implies that  $V(z_{is}) \rightarrow 0$ , resulting in  $z_{is} \approx 1$ . Indeed, the coverage associated with  $\mathbf{z}$  is very high for all scenarios. In cases where data are equidispersed, the model correctly estimates  $z_{is} = 1$ , which is equivalent to a Poisson model. Another characteristic explored in this study concerns the goodness of fit (Table 2). For equidispersed data, models presented very similar performance. When considering overdispersed data, PIG model proved to be advantageous, exhibiting lower WAIC values that were consistent across all scenarios. Tables 2 and 3 show that the RI for PIG and Poisson models when the data were equidispersed had similar performance. In this case, the accuracy of the partition estimates obtained was high, which agrees with our previous discussion. For overdispersed data, Poisson model almost completely lost its clustering capacity, while PIG model provided averaged RI values exceeding 60%. The conclusion drawn from this simulation study is that a PIG model can be applied to both equidispersed and overdispersed data. When overdispersion is not present, PIG model assumes its particular Poisson model case. Therefore, this model can simultaneously deal with estimation and clustering. The opposite does not hold true; when a Poisson model is applied to overdispersed data, the model's clustering capacity decreases drastically. In this case,  $\theta$  attempts to explain the interaction between the cluster-specific intercept and the dispersion parameter, making it difficult for areas to co-cluster.

**Simulation 2 - Exploring the order of temporal dependence and its impact on clustering** All the results mentioned below can be found in Section F.2 of the Appendix. In this case, we fitted PIG models with  $q = 1, 2, \dots, 5$  to all synthetic datasets. Additionally, we fitted a particular case in which partitions were independently sampled. Note that to do this, it is sufficient to fix  $\mathbf{u} = \mathbf{c} = \mathbf{0}$ , thus  $\rho_s$  is independent and identically distributed as  $\text{Be}(v, \kappa)$ . Figure 21 shows that adding a temporal structure to the partition prior tends to enhance the fit performance compared to using the independent version. There was only one scenario in which the model with independent partitions outperformed the others. However, it was unclear which order of dependence yielded the best fit. Looking at the averaged WAIC values (Table 5), the difference between models seems imperceptible, and this occurred similarly in all scenarios. Figure 22 and Table 5 show that the proposed model provided good accuracy in partition estimation, with RI values averaging over 90% for all scenarios. Nonetheless, similar to the WAIC, it is difficult to identify the best order of dependence. On average, the RI values are comparable among the models (Figure 22). Indeed, all parameters used in the temporal structure were estimated similarly across the models, as observed in Table 6.

## 6 An application to dengue data

We applied the proposed model to analyze data described in Section 3 related to dengue cases reported weekly in the Southeast region of Brazil between 2018 and 2023. The response variable  $y_{it}$  represents the number of dengue cases;  $O_{it}$  is the population size (per 100,000 people); and  $\mathbf{X}_{it}$  is the design vector composed of temperature, humidity, and HDI, all measured per area  $i = 1, \dots, 145$  and epidemiological week  $t = 1, \dots, 313$ . The design vector  $\mathbf{V}_{is}$  is composed of temperature and humidity averaged per season (spring, summer, autumn, and winter) in each area, with  $s = 1, \dots, 24$ . We fitted the proposed model (1)–(16) by fixing the prior parameters as follows: for regression coefficients,  $\mu_\beta = \mathbf{0}$  and  $\Sigma_\beta = 10\mathbf{I}$ ; for the cluster- and season-specific parameter,  $a_\theta = b_\theta = 1$ ; we kept  $a_v = 10$ ,  $b_v = 1$ ,  $a_\kappa = 100$ , and  $b_\kappa = 1$  so that the *a priori* expected number of clusters in the first season is around 10% of the total number of areas; and  $a_c = b_c = 1$  so that the *a priori* temporal correlation of the sequence of probabilities is close to zero. For

the MCMC, we saved a sample of size 1,000 by running 15,000 iterations, discarding the first two-thirds as burn-in, and thinning by 5. Convergence was monitored graphically. Prior elicitation and the MCMC algorithm are available in the Appendix, Sections D and E, respectively.

To account for temporal trends, we varied the dependence order parameter  $q$  from 1 to 12, which corresponds to three years. This allowed us to evaluate how different  $q$  values influenced the posterior inference of  $\boldsymbol{\rho}$  and the resulting partition. We also fitted a simpler model assuming independent partitions. Using the WAIC for model selection (see Table 7), we found that a first-order autoregressive structure best fits the dengue data from Southeast Brazil. All results presented in this section from now on were obtained by fitting the proposed model with a dependence order of  $q = 1$ .

Figure 3 displays estimated partitions for each season, where colors differentiate clusters within each partition. Although colors are repeated over time, they do not necessarily represent the same clusters or even relate them. Overall, our model estimated between five and eighteen clusters. Winter was the season with the lowest estimated number of clusters (6 to 9), followed by spring (6 to 13), summer (9 to 14), and autumn, when the largest number of clusters was estimated (5 to 18). This pattern corroborates the temporal trend of the observed data. In Brazil, dengue cases usually begin rising in December and reach their peak between April and May, which corresponds to summer and autumn. In this region, the time from summer to early autumn is characterized by warm and rainy weather, creating suitable conditions for the survival of vectors. The opposite occurs in winter and extends until spring. Additionally, we should consider the mosquito’s lifespan and the time of virus incubation, which may delay the emergence of cases. In general, we observed a greater number of singletons in the partitions estimated for 2023, mainly in autumn and spring. This may be due to the significant increase in the number, scale, and simultaneous occurrence of multiple outbreaks observed in 2023, which spread into regions that were previously unaffected.

Apart from the temporal trend observed in the number of clusters, there is a smooth change in the formation of clusters over time, with no significant variations in their configuration. A spatial pattern of clusters can also be observed when we examine partitions of the same season over years, which may suggest a seasonal dependence. To measure similarity between estimated partitions over time, we calculated the lagged RI values using the `salso` R package, as shown in Figure 23(A). Although the partitions are similar, with an averaged RI of 69%, it is difficult to detect a temporal or even seasonal pattern from the similarity matrix. On the other hand, when examining the estimated values of the probability of removing edges in each season (Figure 23(B)), we observed a certain temporal trend. A pattern repeats itself over the first four years, with a rising trend between spring and autumn, followed by a rising trend between autumn and spring. Additionally, Figure 23(C) shows the autocorrelation function. Recall that we chose the model with  $q = 1$ , so we show the correlation between  $\rho_s$  and  $\rho_{s-1}$ . Figures 23(A)-(C) are presented in the Appendix.

Another important result obtained by fitting our model is the estimated space-time dispersion. To identify which areas and seasons exhibit overdispersed data, we construct dispersion indicators from the posterior distribution of  $\mathbf{z}$  and represent them using maps; see Figure 4. Such indicators point out whether one lies within the 95% credible interval of  $z$  or not. We observed more overdispersion during periods of higher prevalence of dengue. Autumn was the season with the highest level of overdispersion, followed by summer, winter, and spring. For instance, in the autumn of 2023, nearly all areas of Minas Gerais exhibited overdispersion. In contrast, during the winter and spring of 2018, most areas displayed equidispersion. It is important to note that  $z = 1$  is not the only evidence of equidispersion. In the PIG distribution, we have that  $\mathbb{E}(Y_{it} | \lambda_{it}, \psi_{is}) = \mathbb{V}(Y_{it} | \lambda_{it}, \psi_{is})$  whenever  $\mathbb{V}(Z_{is}) = 0$  (see Section 4.1). To further analyze how dispersion changes over time, we selected two areas and calculated the ratio  $\mathbb{E}(Y_{it} | \lambda_{it}, \psi_{is})/\mathbb{V}(Y_{it} | \lambda_{it}, \psi_{is})$ . The first area, Januária, is located in the northern part of the state of Minas Gerais, and its corresponding ratio is shown in Figure 5(C). The second area, Campinas, a significant region in the northwest of the state of São Paulo, is depicted in Figure 5(D). In both regions, we observed that  $\mathbb{V}(Y_{it} | \lambda_{it}, \psi_{is}) > \mathbb{E}(Y_{it} | \lambda_{it}, \psi_{is})$ , which confirms the overdispersion evident in the data. This overdispersion is particularly pronounced in Campinas. Refer to the Appendix for maps of dispersion indicators for all seasons, as well as the temporal evolution of  $\mathbb{E}(Y_{it} | \lambda_{it}, \psi_{is})/\mathbb{V}(Y_{it} | \lambda_{it}, \psi_{is})$  for additional areas.

As presented in (2), the PIG regression model considers two parameters. The spatial-temporal effect of  $\mathbf{z}$ , which accounts for heterogeneity, has already been explored in Figures 4 and 5(C)-(D). Now, we focus on the temporal evolution of  $\boldsymbol{\lambda}$ . In this case,  $\boldsymbol{\lambda}$  depends on temperature and humidity, both of which vary in space

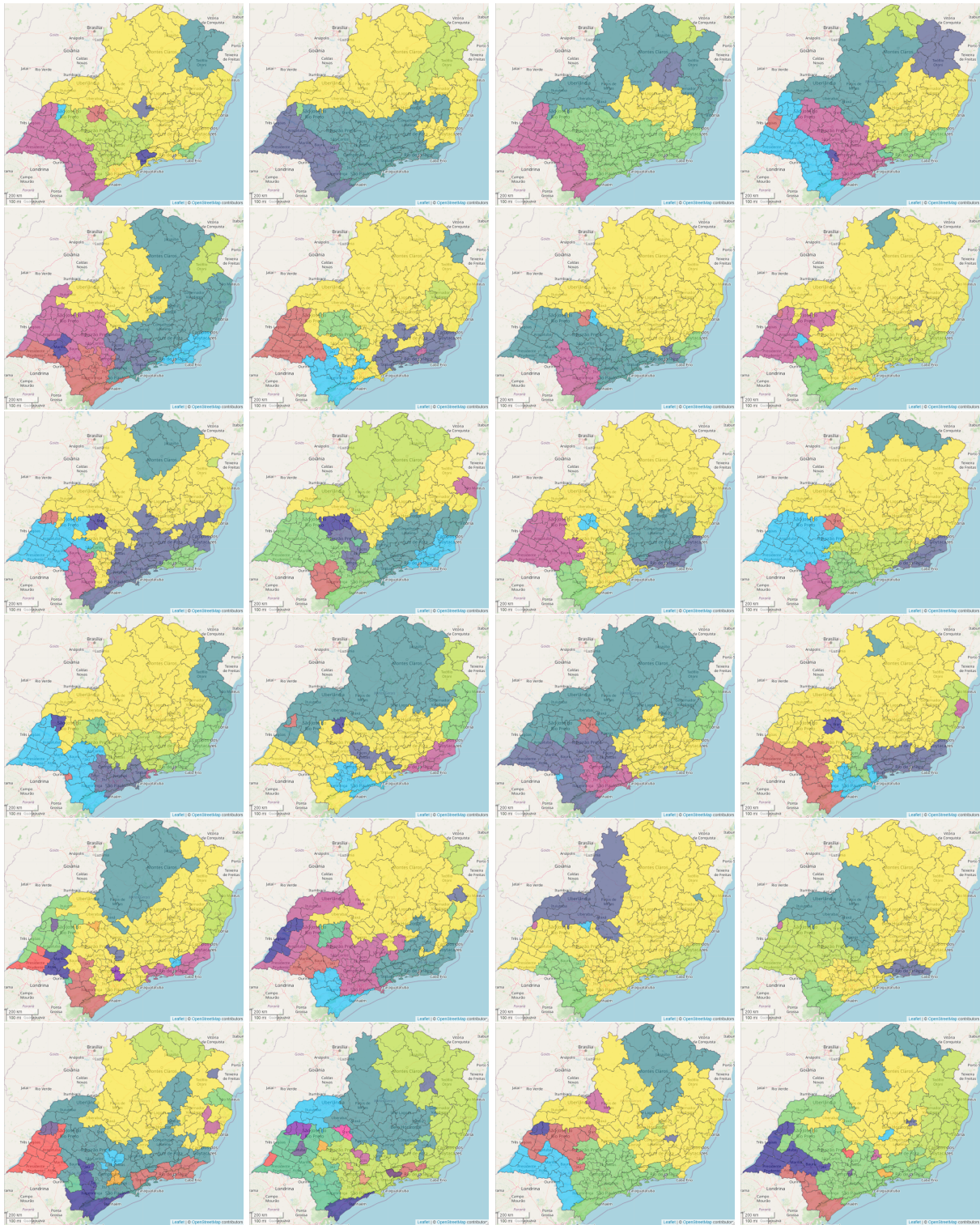


Figure 3: Posterior estimate of the random partition for dengue cases on the Brazilian Southeast region from 2018 (top) to 2023 (bottom) by seasons - summer (1st column), autumn (2nd column), winter (3rd column), and spring (4th column).

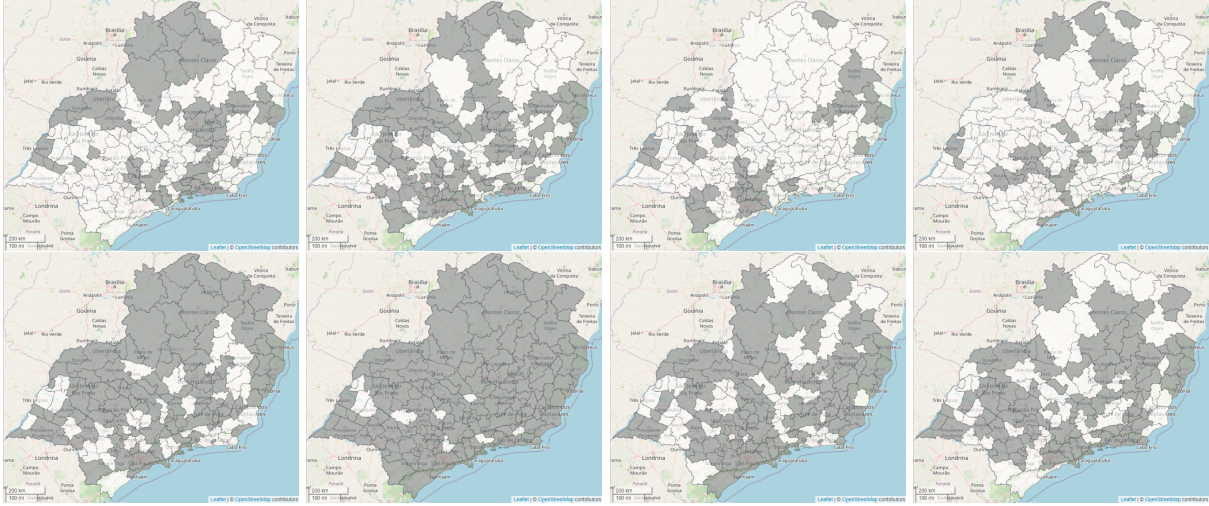


Figure 4: Dispersion indicators by areas constructed from the posterior distribution of  $z$  for 2018 (1st row) and 2023 (2nd row) and seasons - summer (1st column), autumn (2nd column), winter (3rd column), and spring (4th column).  $z \approx 1$  (white);  $z \neq 1$  (gray).

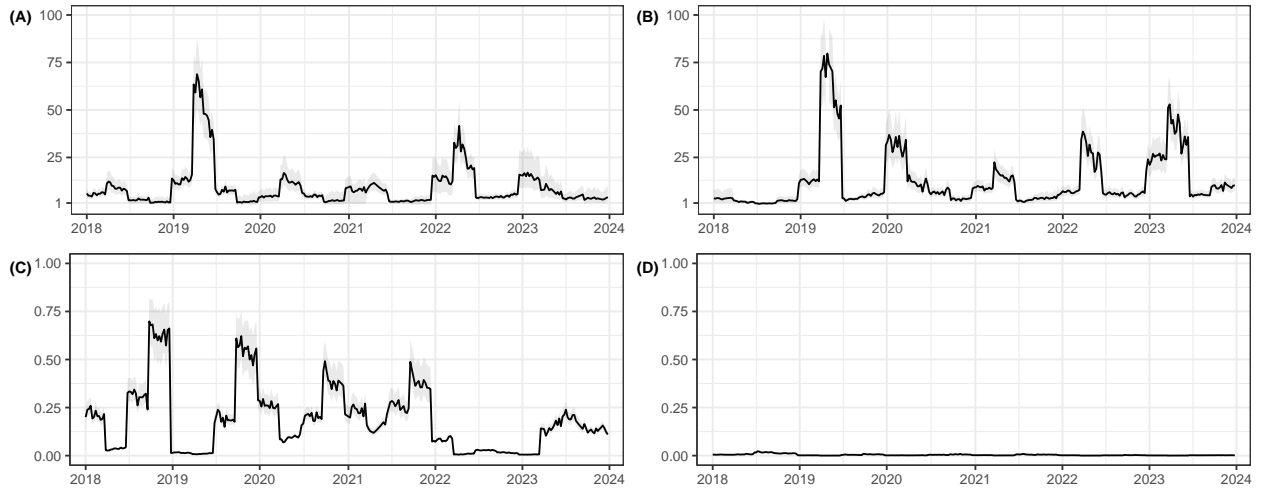


Figure 5: Posterior mean and 95% credible interval of  $\lambda$  (A)-(B) and the ratio  $E(Y_{it} | \lambda_{it}, \psi_{is}) / V(Y_{it} | \lambda_{it}, \psi_{is})$  (C)-(D) over time for two selected area: Januária - MG (left) and Campinas - SP (right).

and time, and on HDI, which varies only in space. To explore the temporal trend of  $\lambda$ , we selected two areas, Januária and Campinas, which have the lowest (0.60) and highest (0.77) observed HDI, respectively. For both regions,  $\lambda$  reached its highest peak in 2019, as shown in Figure 5(A)-(B). Although with less intensity, annual peaks can still be observed. It is worth noting that the cluster-specific parameter  $\theta$  also contributes to explaining  $\lambda$ . Januária and Campinas were estimated to be in the same cluster during four seasons: summer 2019, winter 2020 and 2022, and spring 2022, as illustrated in Figure 3. A graphic representation of the product  $\mathbf{Oz}\lambda$  for these areas can be seen in the Appendix’s Figure 26.

We conclude our analysis by evaluating the regression coefficients considered to explain both the mean and data dispersion. Temperature has a positive effect on both the mean and dispersion, with values of 0.30[0.299, 0.302] and 0.30[0.198, 0.387], respectively. This indicates that a warmer climate contributes to an increase in dengue cases, as well as their heterogeneity. In contrast, humidity has an opposite effect on the mean and dispersion, with values of 0.13[0.124, 0.127] and  $-0.47[-0.469, -0.206]$ , respectively. While higher humidity positively affects the increase in cases, it negatively impacts the dispersion; that is, the increase in cases is more homogeneous over time and space in a humid climate. The HDI was used only to explain the average number of cases, where it has a positive impact of 0.08[0.071, 0.083]. Figure 27 displays the posterior distribution of the regression coefficients.

## 7 Concluding remarks

Motivated by the peculiar characteristics of mosquito-borne disease data and the limited existing literature on spatial-temporal partition modeling, we developed a Bayesian model that incorporates temporal dependence in a series of spatial random partitions. Our approach involves a prior distribution on product partition models and spanning trees. Additionally, we considered a Poisson mixture model to address overdispersion, which is commonly encountered in this field. The proposed model was fitted to analyze both simulated and real data. Through simulation studies, we first demonstrated the necessity of using a model that can effectively capture the overdispersion present in the data. As illustrated in Section F.1 of the Appendix, the PIG model outperforms the Poisson model. Additionally, in Section F.2, we explored the order of temporal dependence and its impact on clustering. We concluded that incorporating a temporal structure into the partition prior generally improves fitting performance compared to the independent version, but the adequate order of temporal dependence is data-specific. In Section 6, we also applied the proposed model to a dataset of dengue cases in the Brazilian Southeast region from 2018 to 2023. Aligned with the specific characteristics of the context, our model accounts for varying spatial partitions across seasons. We considered climate and socio-demographic information as risk factors in order to quantify their effect on disease transmission. This study sheds light on the progression of dengue outbreaks in the region by identifying spatio-temporal clusters, which could aid policymakers in developing effective strategies for disease prevention and control. Another point to highlight is that while our results in the simulation study were robust with respect to the order of dependence, we found more pronounced differences in the application.

The introduction of random spanning trees into PPM for area clustering, combined with the incorporation of a temporal dependence structure in the series of spatial random partitions, is an innovative strategy. Nonetheless, there are still multiple promising opportunities for future research. As discussed in Section 4.2, adopting a sequence of latent variables to define temporal dependence offers benefits, particularly concerning the marginal distribution of  $\rho_s$ , which aids in partition sampling. However, alternative approaches that directly model the original probability vector could be further investigated. Additionally, while our method was developed to model count data, it can be extended to accommodate different types of data by incorporating other distribution families. Another avenue for future research is to explore the less widely studied underdispersion models, which have garnered growing interest in recent years. Finally, the structure could be leveraged more effectively for predictive inference.

## Acknowledgements

Fernando A. Quintana gratefully acknowledges support from the Fondo Nacional de Desarrollo Científico y Tecnológico (FONDECYT) under grant 1220017. Rosangela H. Loschi is partially supported by Conselho Nacional de Desenvolvimento Científico e Tecnológico (CNPq) under grants 405025/2021-1 and 304268/2021-6, and Fundação de Amparo à Pesquisa do Estado de Minas Gerais (FAPEMIG) under grants APQ00674-24 and APQ01748-24.

## References

- Assunção, R. M., Neves, M. C., Câmara, G., and Freitas, C. C. (2006). Efficient regionalization techniques for socio-economic geographical units using minimum spanning trees. *International Journal of Geographical Information Science*, 20(7):797–811.
- Barreto-Souza, W. and Simas, A. B. (2015). General mixed Poisson regression models with varying dispersion. *Statistics and Computing*, 26(6):1263–1280.
- Barry, D. and Hartigan, J. (1993). A Bayesian analysis for change point problems. *Journal of the American Statistical Association*, 88(421):309.
- Caron, F., Neiswanger, W., Wood, F., Doucet, A., and Davy, M. (2017). Generalized Pólya urn for time-varying Pitman-Yor processes. *Journal of Machine Learning Research*, 18:1–32.
- Chen, C., Kim, A. Y., Ross, M., Wakefield, J., and Moise, M. (2023). *SpatialEpi: methods and data for spatial epidemiology*. R package version 1.2.8, <https://CRAN.R-project.org/package=SpatialEpi>.
- Cremaschi, A., Cadonna, A., Guglielmi, A., and Quintana, F. A. (2023). A change-point random partition model for large spatio-temporal datasets. *arXiv:2312.12396*.
- Criscuolo, T. L., Assunção, R. M., Loschi, R. H., Meira Jr., W., and Cruz-Reyes, D. (2023). Handling categorical features with many levels using a product partition model. *The Annals of Applied Statistics*, 17(1):786–814.
- Dahl, D., Johnson, D., and Müller, P. (2020). *salso: search algorithms and loss functions for Bayesian clustering*. R package version 0.2.5, <https://CRAN.R-project.org/package=salso>.
- De Iorio, M., Favaro, S., Guglielmi, A., and Ye, L. (2023). Bayesian nonparametric mixture modeling for temporal dynamics of gender stereotypes. *The Annals of Applied Statistics*, 17(3):2256–2278.
- Dombowsky, A. and Dunson, D. B. (2024). Product centered Dirichlet processes for dependent clustering. *arXiv:2312.05365v2*.
- Duan, L. L. and Dunson, D. B. (2023). Bayesian spanning tree: estimating the backbone of the dependence graph. *Journal of Machine Learning Research*, 24(397):1–44.
- Franklin, L. H., Jones, K. E., Redding, D. W., and Abubakar, I. (2019). The effect of global change on mosquito-borne disease. *The Lancet Infectious Diseases*, 19(9):e302–e312.
- Franzolini, B., De Iorio, M., and Eriksson, J. (2024). Conditional partial exchangeability: a probabilistic framework for multi-view clustering. *arXiv:2307.01152v1*.
- Gelman, A., Hwang, J., and Vehtari, A. (2014). Understanding predictive information criteria for Bayesian models. *Statistics and Computing*, 24:997–1016.
- Giampino, A., Guindani, M., Nipoti, B., and Vannucci, M. (2024). Local level dynamic random partition models for changepoint detection. *arXiv:2407.20085v1*.

- Gutiérrez, L., Mena, R. H., and Ruggiero, M. (2016). A time dependent Bayesian nonparametric model for air quality analysis. *Computational Statistics & Data Analysis*, 95:161–175.
- Hartigan, J. A. (1990). Partition models. *Communications in Statistics - Theory and Methods*, 19(8):2745–2756.
- Hegarty, A. and Barry, D. (2008). Bayesian disease mapping using product partition models. *Statistics in Medicine*, 27(19):3868–3893.
- Hilbe, J. M. (2014). *Modeling Count Data*. Cambridge University Press, Cambridge, UK.
- Hubert, L. and Arabie, P. (1985). Comparing partitions. *Journal of Classification*, 2:193–218.
- Jara, A., Nieto-Barajas, L., and Quintana, F. A. (2013). A time series model for responses on the unit interval. *Bayesian Analysis*, 8(3):723–740.
- Jo, S., Lee, J., Müller, P., Quintana, F. A., and Trippa, L. (2017). Dependent species sampling models for spatial density estimation. *Bayesian Analysis*, 12(2):379–406.
- Jungnickel, D. (2013). *Spanning Trees*, pages 103–134. Springer Berlin Heidelberg.
- Luo, Z. T., Sang, H., and Mallick, B. (2021). A Bayesian contiguous partitioning method for learning clustered latent variables. *Journal of Machine Learning Research*, 22(37):1–52.
- Luo, Z. T., Sang, H., and Mallick, B. (2023). A nonstationary soft partitioned Gaussian process model via random spanning trees. *Journal of the American Statistical Association*, 0:1–12.
- Marinho, R. A., Beserra, E. B., Bezerra-Gusmão, M. A., Porto, V. d. S., Olinda, R. A., and dos Santos, C. A. C. (2016). Effects of temperature on the life cycle, expansion, and dispersion of *Aedes aegypti* (diptera: Culicidae) in three cities in Paraíba, Brazil. *Journal of Vector Ecology*, 41(1):1–10.
- Moraga, P. (2019). *Geospatial health data: modeling and visualization with R-INLA and Shiny*. Chapman & Hall/CRC Biostatistics Series, Boca Raton, US.
- Napier, G., Lee, D., Robertson, C., and Lawson, A. (2018). A Bayesian space–time model for clustering areal units based on their disease trends. *Biostatistics*, 20(4):681–697.
- Page, G. L. and Quintana, F. A. (2016). Spatial product partition models. *Bayesian Analysis*, 11(1):265–298.
- Page, G. L., Quintana, F. A., and Dahl, D. B. (2022). Dependent modeling of temporal sequences of random partitions. *Journal of Computational and Graphical Statistics*, 31(2):614–627.
- Pavani, J. and Quintana, F. A. (2024). A Bayesian multivariate model with temporal dependence on random partition of areal data. *arXiv:2401.08303*.
- Perrakis, K., Karlis, D., Cools, M., and Janssens, D. (2015). Bayesian inference for transportation origin–destination matrices: the Poisson–inverse Gaussian and other Poisson mixtures. *Journal of the Royal Statistical Society. Series A (Statistics in Society)*, 178(1):271–296.
- Quintana, F. A., Loschi, R. H., and Page, G. L. (2018). Bayesian product partition models. *Wiley StatsRef: Statistics Reference Online*, pages 1–15.
- Saraiva, E. F., Vidas, V. P., Flesch, M. V., Gannon, M., and de Bragança Pereira, C. A. (2022). Modeling overdispersed dengue data via Poisson inverse Gaussian regression model: a case study in the city of Campo Grande, MS, Brazil. *Entropy*, 24(9):1256.
- Tam, E., Dunson, D. B., and Duan, L. L. (2024). Exact sampling of spanning trees via fast-forwarded random walks. *arXiv:2405.03096*.

- Teixeira, L. V., Assunção, R. M., and Loschi, R. H. (2015). A generative spatial clustering model for random data through spanning trees. *IEEE International Conference on Data Mining*, pages 997–1002.
- Teixeira, L. V., Assunção, R. M., and Loschi, R. H. (2019). Bayesian space-time partitioning by sampling and pruning spanning trees. *Journal of Machine Learning Research*, 20(85):1–35.
- van Dyk, D. A. and Park, T. (2008). Partially collapsed Gibbs Samplers: theory and methods. *Journal of the American Statistical Association*, 103(482):790–796.
- Zhong, R., Chacón-Montalván, E., and Moraga, P. (2024). Bayesian spatial functional data clustering: applications in disease surveillance. *arXiv:2407.12633v1*.

## Appendix

### A Data description

As stated in Section 3 of the original document, this study was inspired by the analysis of data on tropical diseases. In particular, we focused on examining the incidence of dengue in the 145 microregions of the Brazilian Southeast region. Data were collected on a weekly basis from 2018 to 2023, covering a total of 313 epidemiological weeks. Figure 6 illustrates the time series of dengue cases over the weeks. In total, 5,309,984 cases were reported, reaching their peak in 2019. Figure 7 shows the spatial distribution of SIR calculated using the `SpatialEpi` R package (Chen et al., 2023). Each map represents the geographic distribution of SIR by season between 2018 and 2023. Overall, the areas at the greatest risk for dengue are concentrated in the state of Minas Gerais, with significant variation over time.

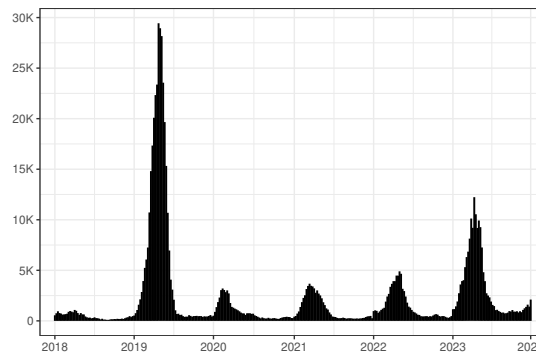


Figure 6: Total number of dengue cases reported per epidemiological week during the years 2018-2023 in the Brazilian Southeast region.

Figure 8 shows the minimum and maximum values of humidity (percentage) and temperature (Celsius degrees) reported weekly during the years 2018-2023 in the Brazilian Southeast region. Maximum humidity values remained very close to or equal to 100% over time. Conversely, minimum values varied greatly, in addition to presenting a seasonal pattern. In general, winter was the driest season, reaching the most extreme values in 2020. At this point, it is important to highlight that, although Brazil is located in both hemispheres (93% of the territory in the Southern Hemisphere and 7% in the Northern Hemisphere), the region under study is in the Southern Hemisphere. Thus, summer occurs from December to March, followed by autumn from March to June, winter from June to September, and finally, spring from September to December.

Considering the seasonal pattern, we mapped the distribution of minimum humidity over the 145 microregions in the Brazilian Southeast in each season, as shown in Figure 9. Areas close to the coast exhibited a wet climate throughout all seasons. The humidity was even more pronounced in the state of Espírito Santo



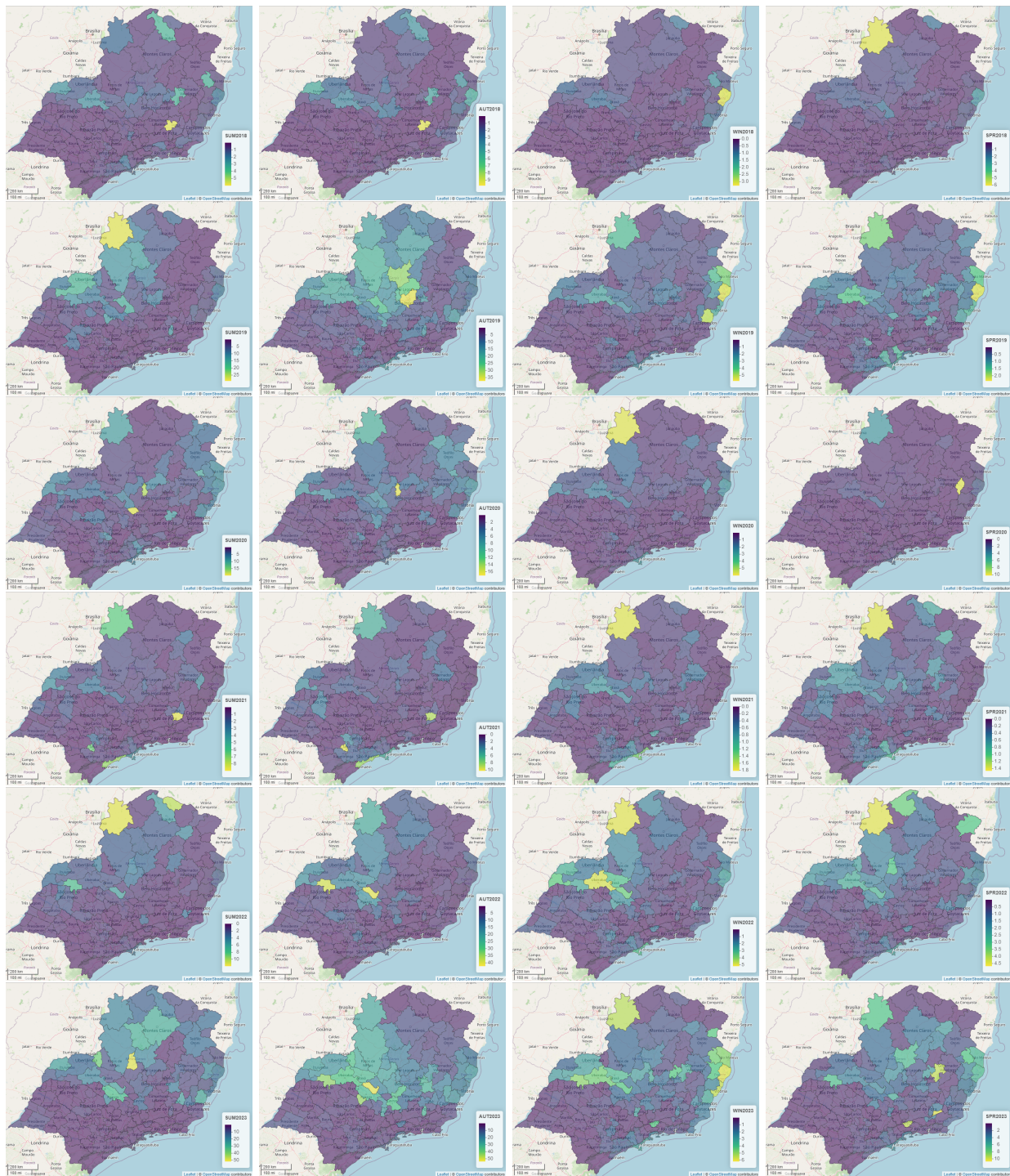


Figure 7: Spatial distribution of standardized incidence ratios of dengue across 145 microregions in the Brazilian Southeast region from 2018 (top) to 2023 (bottom) by seasons - summer (1st column), autumn (2nd column), winter (3rd column), and spring (4th column).

and to the north of Rio de Janeiro. The opposite was observed in the Northwest of São Paulo, where low

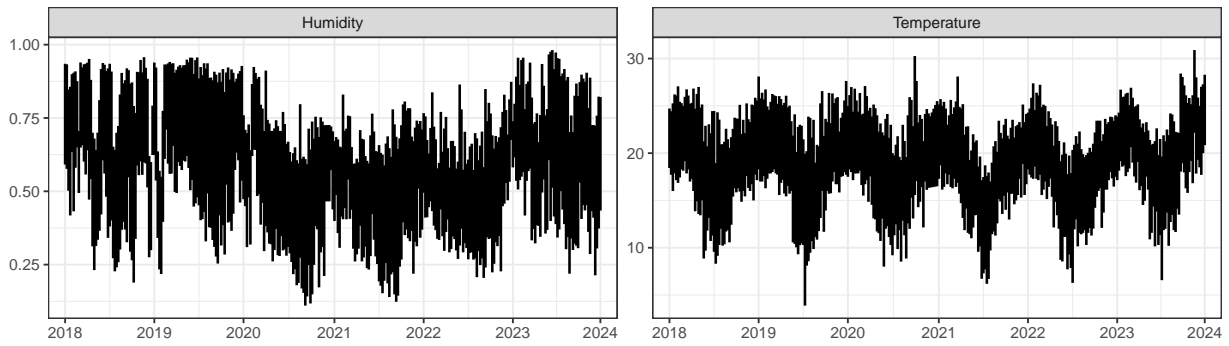


Figure 8: Minimum and maximum humidity (percentage) and temperature (Celsius degree) reported weekly in the Brazilian Southeast region during the years 2018-2023.

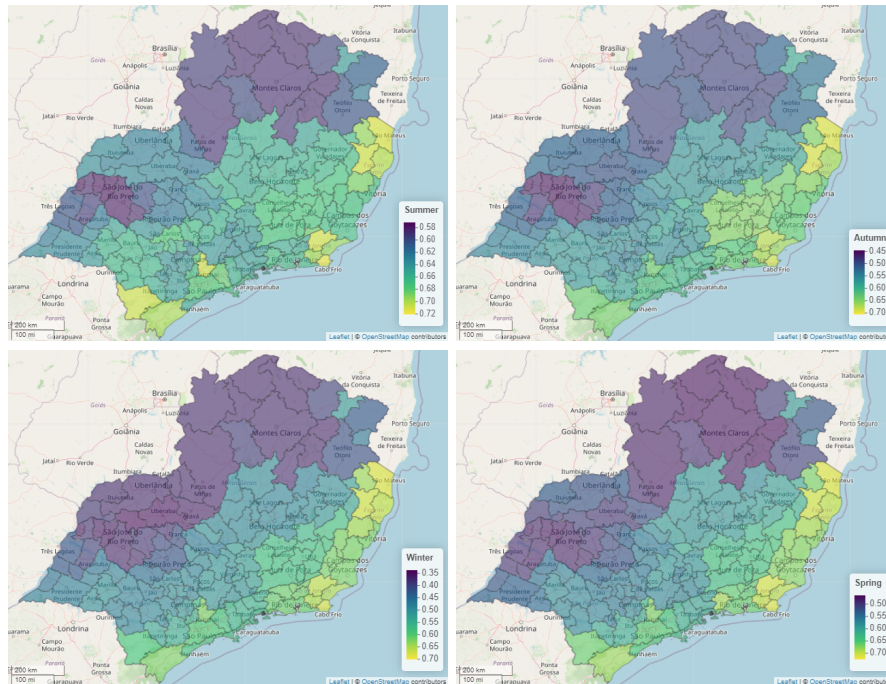


Figure 9: Spatial distribution of minimum humidity over the 145 microregions in the Brazilian Southeast in each season. Average values were obtained by considering the years 2018-2023.

humidity was noted throughout the year. The North and West of the state of Minas Gerais were also arid regions. Regarding temperature, there was significant temporal variation for both minimum and maximum values, as demonstrated in Figure 8. Additionally, a seasonal pattern was clearly observed. As naturally expected, the lowest temperatures occurred in winter, especially in July 2019 when temperatures below 5°C were recorded. The highest temperatures were recorded in the last week of September and the first week of October 2020, reaching nearly 40°C. The spatial distribution of minimum temperature over the 145 microregions in the Brazilian Southeast in each season is depicted in Figure 10. The state of Espírito Santo and Northwestern São Paulo are areas where the highest temperatures were recorded, which remained consistent across all seasons.

On the other hand, the lowest temperatures were recorded in southeastern Minas Gerais and southern São

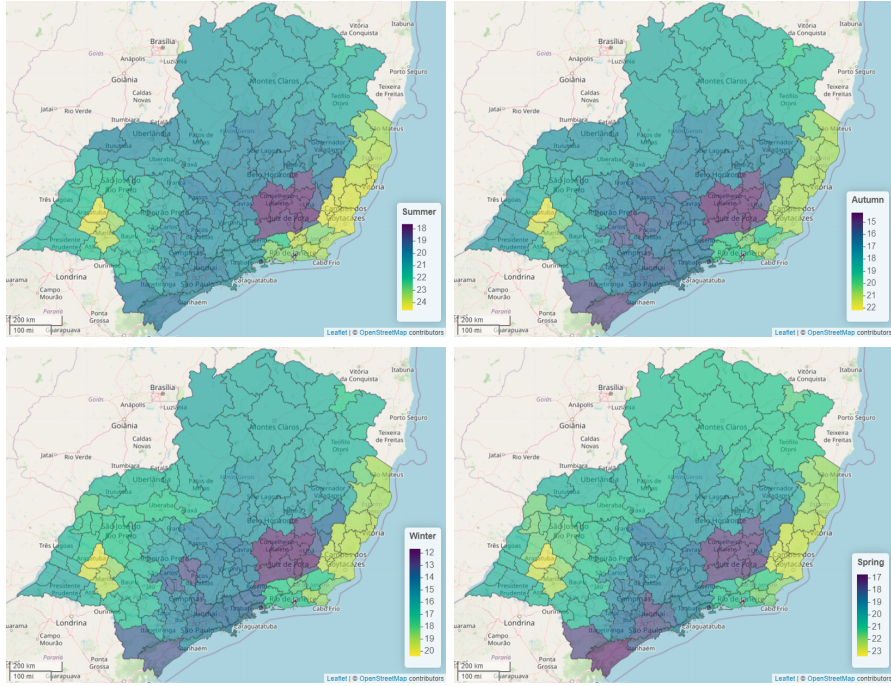


Figure 10: Spatial distribution of minimum temperature across the 145 microregions in the Brazilian South-east during each season. Average values were obtained by considering the years 2018-2023.

Paulo. As shown in Figures 8, 9, and 10, humidity and temperature were not homogeneous across the region, or even within each state. They varied greatly over time, with the exception of maximum humidity, which remained almost constant. To account for their variability over time, we used minimum temperature and minimum humidity as spatio-temporal covariates in this study.

Finally, Figure 11 illustrates the spatial distribution of HDI in the study region, showing a clear pattern. Areas in the northern part of the region, particularly those in Minas Gerais bordering Bahia, have lower HDI values. Conversely, higher HDI values are concentrated in the southern part of the region, particularly in the state of São Paulo. It is worth mentioning that the Southeast region is the most developed in Brazil, exhibiting a smooth variation in HDI values.

## B Key concepts

The proposed model is built assuming that our map containing  $n$  areas is represented by an undirected graph. In this section, we provide some preliminary concepts that are assumed throughout the model formulation in the main manuscript.

### B.1 Spanning tree

To improve comprehension of spanning trees (ST), let us review some key concepts from graph theory. A graph is an ordered pair  $G = (V, E)$  comprising a set  $V$  of vertices or nodes connected by edges in set  $E$ . An edge,  $e = (v_i, v_j)$ , connecting vertices  $v_i$  and  $v_j$  indicates that those vertices are adjacent to each other or, in a spatial context, that they are neighbors. A graph is said to be connected if, for any pair of nodes  $v_i$  and  $v_j$ , there is at least one path connecting them. It may also contain circuits, i.e., paths that start and end at the same vertex. Graphs can be directed or undirected, depending on whether there is an order among the vertices. Figure 12, left and center, respectively, illustrates these concepts.

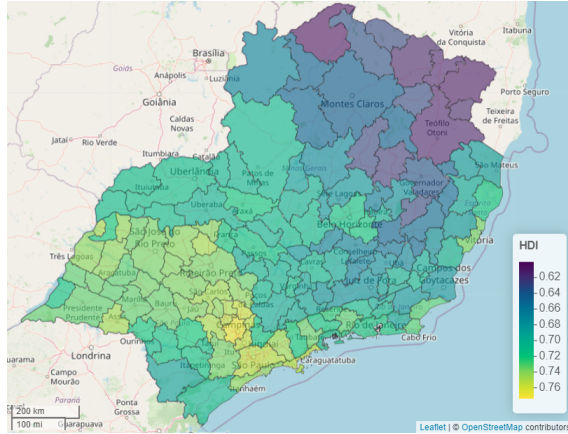


Figure 11: Spatial distribution of the Human Development Index across the 145 microregions in the Brazilian Southeast region. Information is based on the 2010 Demographic Census.

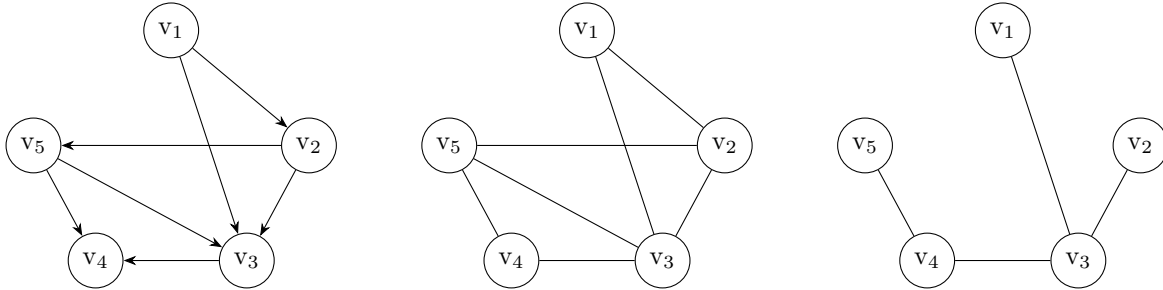


Figure 12: Different graph types: directed (left), undirected (center), tree (right).

A *spanning tree* of an undirected connected graph is a subgraph that includes all the nodes of  $G$  but only some of its edges, as shown in Figure 12 (right). In other words, in the spanning tree, any two nodes in the graph are connected by a unique path. Thus, a tree with  $n$  vertices has exactly  $n - 1$  edges. Many trees can be generated from the same graph; however, in this study, we consider the minimum spanning tree, which is a tree with the minimum possible total edge weight.

A partition of the map is induced by removing some edges from the spanning tree such that the vertices connected by the remaining edges form clusters. Figure 13 shows a spanning tree and two different partitions induced by removing one and two edges, at the center and left, respectively. It is important to note that there is a significant advantage to clustering from a spanning tree instead of from the original graphs, as the search space of partitions is reduced. Figure 12 illustrates this. While the vertices in the undirected graph are connected by seven edges, the tree has only four edges, as shown in Figure 12 (center and right, respectively).

## B.2 On the prior for the number of clusters

It is not difficult to see from the proposed model (see Eq.(8)–(10) of the main manuscript) that the prior distribution of  $\rho_s$  can induce higher or lower levels of informativity for the prior distribution of  $\pi_s$  based on prior knowledge about the number of clusters. Therefore, it would be more relevant to obtain prior marginal distributions for partition, the probability of removing edges, and the number of clusters. This will help in the prior elicitation of parameters. To do so, let  $N_{\mathcal{T}_s}$  be the total number of spanning trees associated with a certain graph,  $N_{\mathcal{T}_s}(\pi_s)$  be the total number of spanning trees compatible with the partition  $\pi_s$ , and  $K_s$

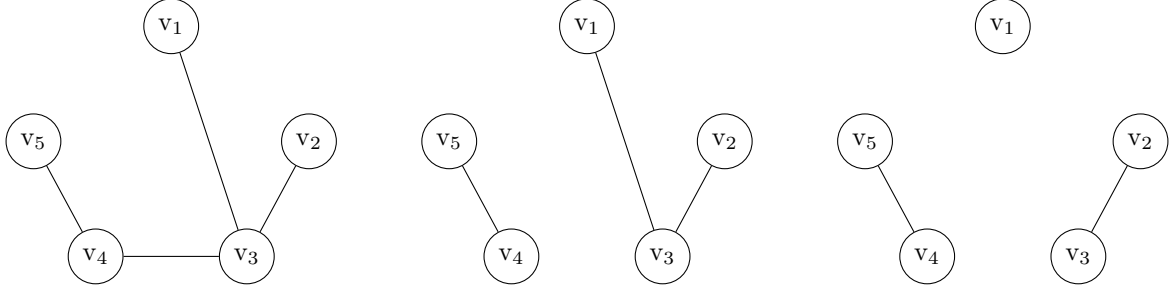


Figure 13: Spanning tree (left) and the two (center) and three clusters (right) partitions generated from it.

be the number of clusters in season  $s$ . Consider the prior distribution  $\mathbb{P}[\boldsymbol{\pi}_s \mid \mathcal{T}_s, \rho_s]$  defined in Eq.(8) of the main manuscript. Then, we have:

$$\begin{aligned}
\mathbb{P}[\boldsymbol{\pi}_s \mid \rho_s, u_s, \dots, u_{s-q}] &= \sum_{\mathcal{T}_s} \mathbb{P}[\boldsymbol{\pi}_s \mid \mathcal{T}_s, \rho_s] \mathbb{P}[\mathcal{T}_s] \\
&= \sum_{\mathcal{T}_s} \rho_s^{k_s-1} (1 - \rho_s)^{n-k_s} \mathbb{P}[\mathcal{T}_s] \mathbb{1}_{[\boldsymbol{\pi}_s \prec \mathcal{T}_s]} \\
&= \rho_s^{k_s-1} (1 - \rho_s)^{n-k_s} \frac{N_{\mathcal{T}_s}(\boldsymbol{\pi}_s)}{N_{\mathcal{T}_s}}
\end{aligned}$$

and

$$\begin{aligned}
\mathbb{P}[K_s = k_s \mid \rho_s] &= \sum_{\boldsymbol{\pi}_s} \mathbb{P}[\boldsymbol{\pi}_s \mid \rho_s, u_s, \dots, u_{s-q}] \mathbb{1}_{[\boldsymbol{\pi}_s, k_s]} \\
&= \binom{n-1}{k_s-1} \rho_s^{k_s-1} (1 - \rho_s)^{n-k_s} \frac{N_{\mathcal{T}_s}(\boldsymbol{\pi}_s)}{N_{\mathcal{T}_s}},
\end{aligned}$$

where  $\mathbb{1}_{[\boldsymbol{\pi}_s, k_s]}$  indicates partitions  $\boldsymbol{\pi}_s$  formed by  $k_s$  clusters (Teixeira et al., 2019).

Considering the prior distribution  $\mathbb{P}[\rho_s \mid u_s, \dots, u_{s-q}]$  as shown in Eq.(10) of the main manuscript, we know from Jara et al. (2013) that  $\rho_s$  is marginally distributed as Beta( $v, \kappa$ ). To see this result, note that from Eq.(11) of the main manuscript, it follows that:

$$\sum_{l=0}^q u_{s-l} \mid w \sim \text{Bin} \left( \sum_{l=0}^q c_{s-l}, w \right),$$

thus, we have that its marginal distribution is given by:

$$\begin{aligned}
\mathbb{P} \left[ \sum_{l=0}^q u_{s-l} \right] &= \int_0^1 \mathbb{P}[u_s, \dots, u_{s-q} \mid w] \mathbb{P}[w] \partial w \\
&= \binom{\sum_{l=0}^q c_{s-l}}{\sum_{l=0}^q u_{s-l}} \frac{\Gamma(v + \kappa)}{\Gamma(v)\Gamma(\kappa)} \int_0^1 w^{\sum_{l=0}^q u_{s-l} + v - 1} (1-w)^{\sum_{l=0}^q (c_{s-l} - u_{s-l}) + \kappa - 1} \\
&= \binom{\sum_{l=0}^q c_{s-l}}{\sum_{l=0}^q u_{s-l}} \frac{\Gamma(v + \kappa)}{\Gamma(v)\Gamma(\kappa)} \frac{\Gamma \left( v + \sum_{l=0}^q u_{s-l} \right) \Gamma \left( \kappa + \sum_{l=0}^q (c_{s-l} - u_{s-l}) \right)}{\Gamma \left( v + \kappa + \sum_{l=0}^q c_{s-l} \right)},
\end{aligned}$$

which is the density of the BeBin $\left(v, \kappa, \sum_{l=0}^q c_{s-l}\right)$ . Then, we obtain the marginal distribution of  $\rho_s$  by doing:

$$\begin{aligned}
\mathbb{P}[\rho_s] &= \sum_u \mathbb{P}[\rho_s \mid u_s, \dots, u_{s-q}] \mathbb{P}\left[\sum_{l=0}^q u_{s-l}\right] \\
&= \sum_u \frac{\Gamma\left(v + \kappa + \sum_{l=0}^q c_{s-l}\right)}{\Gamma\left(v + \sum_{l=0}^q u_{s-l}\right) \Gamma\left(\kappa + \sum_{l=0}^q (c_{s-l} - u_{s-l})\right)} \rho_s^{v + \sum_{l=0}^q u_{s-l} - 1} (1 - \rho_s)^{\kappa + \sum_{l=0}^q (c_{s-l} - u_{s-l}) - 1} \\
&\quad \times \left(\sum_{l=0}^q c_{s-l}\right) \frac{\Gamma(v + \kappa)}{\Gamma(v)\Gamma(\kappa)} \frac{\Gamma\left(v + \sum_{l=0}^q u_{s-l}\right) \Gamma\left(\kappa + \sum_{l=0}^q (c_{s-l} - u_{s-l})\right)}{\Gamma\left(v + \kappa + \sum_{l=0}^q c_{s-l}\right)} \\
&= \frac{\Gamma(v + \kappa)}{\Gamma(v)\Gamma(\kappa)} \rho_s^{v-1} (1 - \rho_s)^{\kappa-1} \sum_u \left(\sum_{l=0}^q c_{s-l}\right) \rho_s^{\sum_{l=0}^q u_{s-l}} (1 - \rho_s)^{\sum_{l=0}^q (c_{s-l} - u_{s-l})} \\
&= \frac{\Gamma(v + \kappa)}{\Gamma(v)\Gamma(\kappa)} \rho_s^{v-1} (1 - \rho_s)^{\kappa-1},
\end{aligned}$$

which concludes the proof that  $\rho_s$  is marginally distributed as Beta( $v, \kappa$ ). This result is crucial for determining the marginal distributions of both the partition  $\boldsymbol{\pi}_s$  and the number of clusters  $k_s$ . After taking everything discussed into account, we finally have:

$$\begin{aligned}
\mathbb{P}[\boldsymbol{\pi}_s] &= \int_0^1 \mathbb{P}[\boldsymbol{\pi}_s \mid \rho_s] \mathbb{P}[\rho_s] \partial \rho_s = \int_0^1 \rho_s^{k_s-1} (1 - \rho_s)^{n-k_s} \frac{N_{\mathcal{T}_s}(\boldsymbol{\pi}_s)}{N_{\mathcal{T}_s}} \frac{\Gamma(v + \kappa)}{\Gamma(v)\Gamma(\kappa)} \rho_s^{v-1} (1 - \rho_s)^{\kappa-1} \partial \rho_s \\
&= \frac{N_{\mathcal{T}_s}(\boldsymbol{\pi}_s)}{N_{\mathcal{T}_s}} \frac{\Gamma(v + \kappa)}{\Gamma(v)\Gamma(\kappa)} \frac{\Gamma(k_s + v - 1)\Gamma(n - k_s + \kappa)}{\Gamma(v - 1 + n + \kappa)}
\end{aligned}$$

and

$$\begin{aligned}
\mathbb{P}[K_s = k_s] &= \int_0^1 \mathbb{P}[K_s = k_s \mid \rho_s] \mathbb{P}[\rho_s] \partial \rho_s \\
&= \int_0^1 \binom{n-1}{k_s-1} \rho_s^{k_s-1} (1 - \rho_s)^{n-k_s} \frac{N_{\mathcal{T}_s}(\boldsymbol{\pi}_s)}{N_{\mathcal{T}_s}} \frac{\Gamma(v + \kappa)}{\Gamma(v)\Gamma(\kappa)} \rho_s^{v-1} (1 - \rho_s)^{\kappa-1} \partial \rho_s \\
&= \binom{n-1}{k_s-1} \frac{N_{\mathcal{T}_s}(\boldsymbol{\pi}_s)}{N_{\mathcal{T}_s}} \frac{\Gamma(v + \kappa)}{\Gamma(v)\Gamma(\kappa)} \frac{\Gamma(k_s + v - 1)\Gamma(n - k_s + \kappa)}{\Gamma(v - 1 + n + \kappa)}. \tag{17}
\end{aligned}$$

Although the prior distribution of  $k_s$  depends on the graph topology through  $\frac{N_{\mathcal{T}_s}(\boldsymbol{\pi}_s)}{N_{\mathcal{T}_s}}$ , given a tree compatible with the partition, the expected number of clusters *a priori* is not dependent. Furthermore, note that Eq.(17) corresponds to the beta-binomial density, whose parameters are the same as those used in the marginal distribution of  $\rho_s$ , in addition to the number of edges in the tree, i.e., BeBin( $k_s - 1; n - 1, v, \kappa$ ). Having identified this, we can obtain the mean and variance of  $k_s$  by:

$$\mathbb{E}(k_s \mid \cdot) = (n - 1) \frac{v}{v + \kappa} + 1, \tag{18}$$

$$\mathbb{V}(k_s \mid \cdot) = (n - 1) \frac{v\kappa(v + \kappa + n - 1)}{(v + \kappa)^2(v + \kappa + 1)}. \tag{19}$$

This finding is important for prior elicitation because it shows that  $\rho_s$  directly influences the number of clusters through its hyperparameters  $v$  and  $\kappa$ . As an illustration, we calculated the mean and variance of

$\nu$ \ $\kappa$	0.01	1	5	10	15	20	25	30
0.01	36 / 1167	69 / 24	70 / 2	70 / 0	70 / 0	70 / 0	70 / 0	70 / 0
1	2 / 24	36 / 408	58 / 103	64 / 38	66 / 20	67 / 13	67 / 9	68 / 7
10	1 / 1	37 / 38	24 / 80	36 / 73	42 / 60	47 / 49	50 / 41	53 / 34
20	1 / 1	34 / 13	15 / 40	24 / 49	31 / 49	36 / 46	39 / 42	42 / 39
30	1 / 1	33 / 7	11 / 24	18 / 34	24 / 38	29 / 39	32 / 38	36 / 36
40	1 / 1	33 / 4	9 / 17	15 / 26	20 / 30	24 / 32	28 / 33	31 / 33
50	1 / 1	32 / 3	7 / 13	12 / 20	17 / 25	21 / 28	24 / 29	27 / 30
60	1 / 1	32 / 2	6 / 10	11 / 17	15 / 21	18 / 24	21 / 26	24 / 27
70	1 / 1	32 / 2	6 / 8	10 / 14	13 / 18	16 / 21	19 / 23	22 / 24
80	1 / 1	32 / 2	5 / 7	9 / 12	12 / 16	15 / 18	17 / 21	20 / 22
90	1 / 1	32 / 1	5 / 6	8 / 10	11 / 14	14 / 17	16 / 19	18 / 20
100	1 / 1	32 / 1	4 / 5	7 / 9	10 / 12	12 / 15	15 / 17	17 / 19
110	1 / 1	32 / 1	4 / 5	7 / 8	9 / 11	12 / 14	14 / 16	16 / 17
120	1 / 1	32 / 1	4 / 4	6 / 7	9 / 10	11 / 13	13 / 14	15 / 16
130	1 / 1	32 / 1	4 / 4	6 / 7	8 / 9	10 / 12	12 / 13	14 / 15
140	1 / 1	31 / 1	3 / 3	6 / 6	8 / 9	10 / 11	11 / 13	13 / 14
150	1 / 1	31 / 1	3 / 3	5 / 6	7 / 8	9 / 10	11 / 12	12 / 13

Table 1: Number of cluster *a priori* (mean/variance) for different specifications of  $\nu$  and  $\kappa$ .

the expected number of clusters by considering the 70 areas of the map. Table 1 displays the values found for different specifications of  $\nu$  and  $\kappa$ .

### B.3 Autocorrelation function

As discussed in Section 4.2 of the main manuscript, one advantage of using this approach lies in the calculation of the temporal autocorrelation of  $\{\rho_s\}$ . This function depends on the parameters  $\nu$ ,  $\kappa$ , and  $\{c_s\}$ . Thus, any prior knowledge about this autocorrelation may assist in the prior elicitation of these parameters. To set the hyperparameters of  $\zeta$ , for instance, we computed the autocorrelation function of  $\{\rho_s\}$  for some values of  $\nu$ ,  $\kappa$ , and  $\{c_s\}$ . Figure 14(A) displays autocorrelation values obtained by varying  $\nu$  and  $\kappa$ , while  $\{c_s\} = 1$  is kept fixed. In contrast, Figure 14(B) illustrates the autocorrelation values obtained by fixing  $\nu = \kappa = 1$  and varying hyperparameter  $\zeta$ . In this case, it is evident that the values of  $\{c_s\}$  have a significant impact on autocorrelation, whereas  $\nu$  and  $\kappa$  do not appear to play a significant role. As noted in the model formulation, the time dependence of the partition sequence is driven by time dependence of  $\rho_s$ . This connection, illustrated in Figure 2 of the main manuscript, highlights the importance of the correlation among  $\rho_s$ .

Additionally, within each season, the correlation among observations is indirect, as they share common parameters ( $\theta$  and  $z$ ). To analyze the data autocorrelation, we begin by generating probability vectors based on prior distributions with different hyperparameter values. Next, using these probabilities, we create random partitions and subsequently produce synthetic data. Finally, we assess the autocorrelation using a standard autocorrelation function. To do so, let us set  $\nu = 10$  and  $\kappa = 100$  so that, according to Table 1, the *a priori* expected number of clusters in the first season is around 10% of the total number of areas. Then, we randomly generate  $\{c_s\}$  from its prior distribution with  $\zeta = 1, 10, 50, 100$ . See Section F for the generation settings of the other model components. Once we have the dataset, we calculate the correlation function using `acf` R function.

Figure 15 displays the autocorrelation function of  $\{y_t\}$  for different areas. It is difficult to determine whether the correlation observed in the data is influenced by the correlation of  $\{\rho_s\}$ , even though the partition has a direct impact on the data through  $\theta$  values. However, it is unquestionable that the data are autocorrelated over time. Furthermore, we can observe a seasonal trend, which can be derived from cluster parameters, dispersion parameters, or covariates. It is also worth noting that, in order to keep the expected

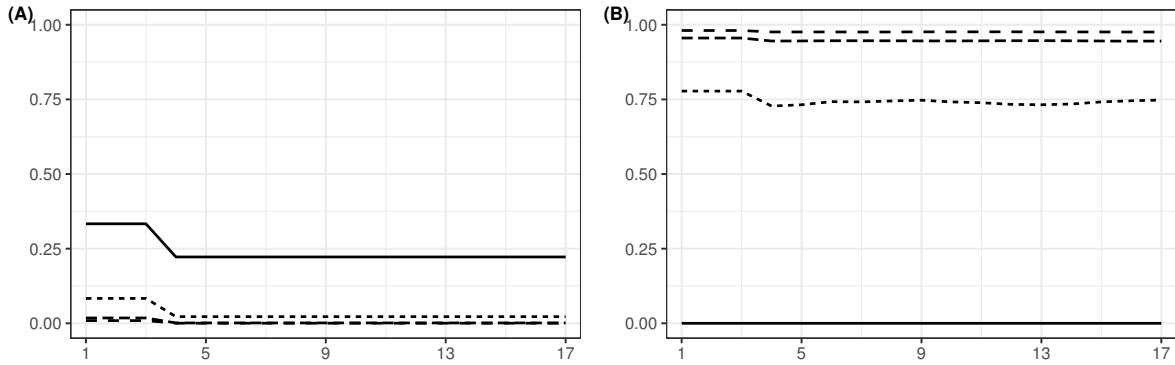


Figure 14: Autocorrelation function of  $\{\rho_s\}$  for  $q = 3$ ,  $s = 1$ , and  $l = 1, \dots, 17$ . (A) Values obtained by fixing  $\{c_s\} = 1$  and varying  $v$  and  $\kappa$ , with  $v = \kappa = 1$  (solid line),  $v = 1, \kappa = 5$  (dotted line),  $v = 5, \kappa = 50$  (dashed line), and  $v = 10, \kappa = 100$  (longdashed line). (B) Values obtained by fixing  $v = \kappa = 1$  and randomly generating  $\{c_s\}$  from the prior distribution with  $\zeta = 1$  (solid line),  $\zeta = 10$  (dotted line),  $\zeta = 50$  (dashed line), and  $\zeta = 100$  (longdashed line).

number of clusters reasonably small, the values of  $\rho$  must remain low, therefore, assuming  $\zeta = 50$  or  $\zeta = 100$  is unrealistic for data analysis as it encourages a large number of clusters.

## C Posterior Inference

Although posterior inference is analytically intractable for this model, the fact that some full conditionals follow known distributions simplifies the sampling process. The parameters  $\theta_{js}^*$ ,  $z_{is}$ ,  $\rho_s$ ,  $w$ , and  $\zeta$  are sampled via the usual Gibbs sampler algorithm, and a Metropolis-within-Gibbs algorithm is used to sample from the posteriors of  $\beta$ ,  $\delta$ ,  $u$ ,  $c$ ,  $v$ , and  $\kappa$ .

The most challenging step is sampling from the posterior of  $(\pi_s, \mathcal{T}_s)$ . We implement a Gibbs sampler algorithm to explore the space of spanning trees and partitions induced by removing the edges. This section focuses on detailing the last two sampling processes - for the partition and the tree - which are the most time-consuming computations. Nonetheless, the complete pseudocode may be found in Section E

### C.1 Sampling the partition

Proposed by Teixeira et al. (2015), the Gibbs algorithm used to sample from the posterior of the random partitions given a compatible spanning tree is based on the strategy of Barry and Hartigan (1993). Adapted to the graph context, each coordinate of this binary vector represents an edge, and its dimension is the number of edges in the spanning tree, i.e.,  $n - 1$ . If the vector coordinate is 0, the edge must be removed from the tree to form the partition. Otherwise, the edge must not be removed. Thus, samples from the posterior distribution of the partition can be obtained by sampling from the posterior distribution of the binary vector by means of the usual Gibbs sampler algorithm. Let  $\nu = (\nu_1, \dots, \nu_{(n-1)})$  be the binary representation of a partition  $\pi$ , and let  $\Omega$  denote the complete parameter vector. The probability of removing an edge can be obtained based on its full conditional probability  $\mathbb{P}[\nu_l | \nu_{-l}, \Omega, \mathbf{Y}]$ , where  $\nu_{-l} = (\nu_1, \dots, \nu_{(l-1)}, \nu_{(l+1)}, \dots, \nu_{(n-1)})$ . Since the variable  $\nu_l$  can assume only two values, it is sufficient to compute the ratio between them, which is formulated as:

$$R_l = \frac{\mathbb{P}[\nu_l = 1 | \nu_{-l}, \Omega, \mathbf{Y}]}{\mathbb{P}[\nu_l = 0 | \nu_{-l}, \Omega, \mathbf{Y}]} = \frac{\mathbb{P}[\pi^{(1)} | \Omega, \mathbf{Y}]}{\mathbb{P}[\pi^{(0)} | \Omega, \mathbf{Y}]}, \quad (20)$$

where  $\pi^{(1)}$  represents the partition without any changes and  $\pi^{(0)}$  is the new partition obtained by removing the  $l$ -th edge. Note that the numerator and denominator differ only at position  $l$ . By removing edge  $l$ ,



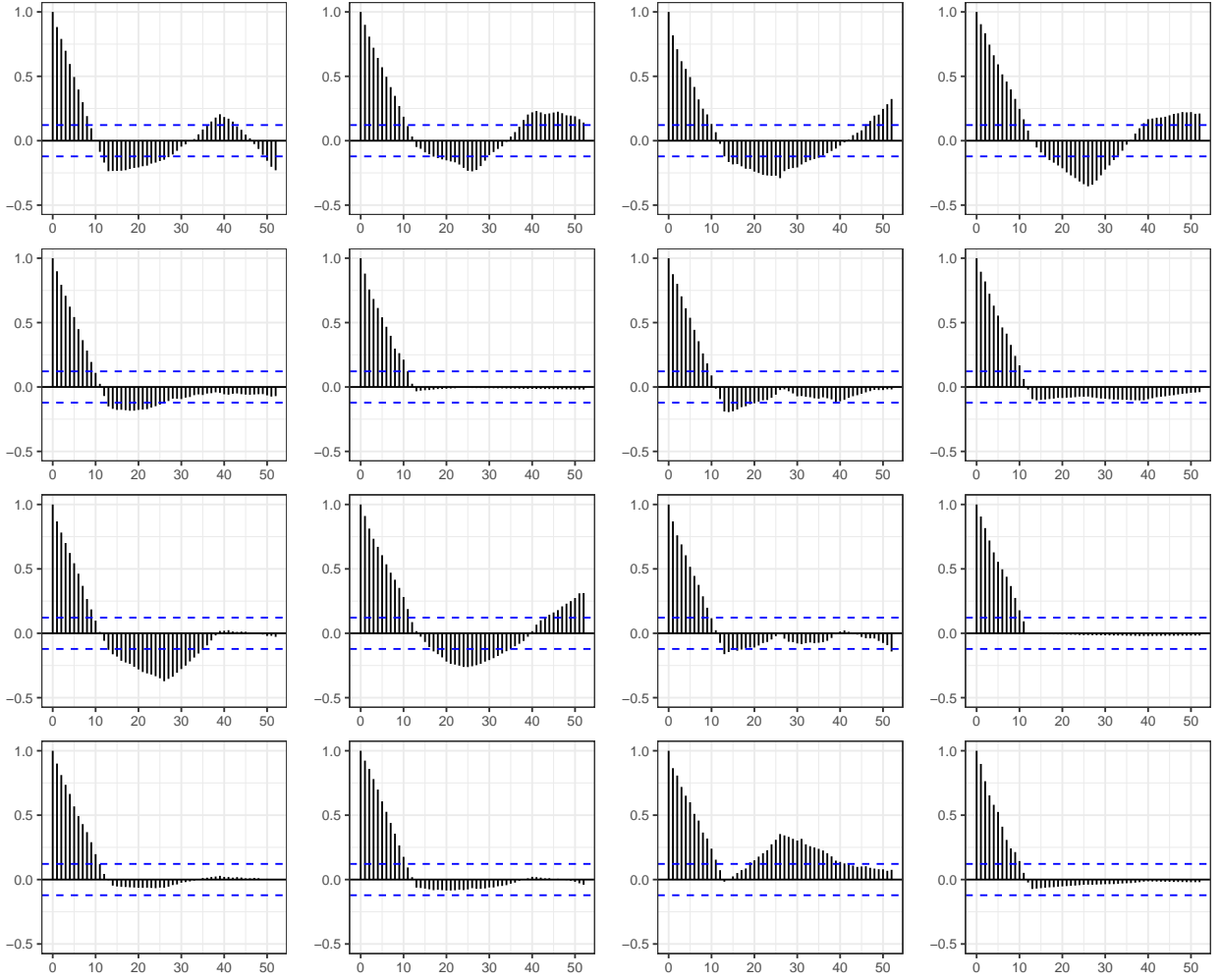


Figure 15: Autocorrelation function of  $\{y_t\}$  for different areas represented in the rows. Data generated with different  $\zeta$  values is represented in the columns (from left to right:  $\zeta = 1, 10, 50, 100$ ).

the cluster containing the areas connected by this edge is split into two new clusters. These two different partitions induce a different number of clusters, which implies distinct coordinates in  $\theta^*$  in the numerator and denominator, making it unfeasible to run a standard Gibbs sampler. To solve this problem, we integrate over  $\theta^*$  in (20). This calculation is straightforward since the full conditional of  $\theta^*$  is a well-known distribution. Additionally, all the other clusters remain unchanged. This modified Gibbs sampler can be defined as a partially collapsed Gibbs sampler (van Dyk and Park, 2008). To achieve faster convergence of the MCMC algorithm, we also integrate  $\rho$  out from (20). By doing this, we reduce instability in the algorithm by eliminating potential divisions by zero.

For the proposed model formulated in Section 4 of the main manuscript, after integrating out  $\theta^*$  and  $\rho$ , the ratio for season  $s$  is:

$$R_{ls} = \frac{\left( n - k_s + \kappa + \sum_{l=0}^q (c_{s-l} - u_{s-l}) - 1 \right) \Gamma(a)}{\left( k_s + v + \sum_{l=0}^q u_{s-l} - 1 \right) b^a} \frac{f_s^{(1)}(\mathbf{Y}_{S_j})}{f_s^{(0)}(\mathbf{Y}_{S_j}^{(1)}) f_s^{(0)}(\mathbf{Y}_{S_j}^{(2)})},$$

where  $f_s(\mathbf{Y}_{S_j})$  denotes the normalizing constant obtained when integrating  $\boldsymbol{\theta}^*$  out, and is given by

$$f_s(\mathbf{Y}_{S_j}) = \frac{\Gamma\left(a + \sum_{i \in S_j} \sum_{t \in s} y_{it}\right)}{\left(b + \sum_{i \in S_j} z_{is} \sum_{t \in s} O_{it} \exp\{X_{it}^\top \beta\}\right) \binom{a + \sum_{i \in S_j} \sum_{t \in s} y_{it}}{}}.$$

Here, function  $f_s^{(1)}(\mathbf{Y}_{S_j})$  is related to the whole cluster, whereas  $f_s^{(0)}(\mathbf{Y}_{S_j}^{(1)})$  and  $f_s^{(0)}(\mathbf{Y}_{S_j}^{(2)})$  are computed from the two sub-clusters formed when the  $l$ -th edge is removed from the tree. Once  $R_{l_s}$  is obtained,  $\nu_l$  can be updated by a Metropolis-within-Gibbs step with a uniformly generated candidate.

## C.2 Sampling the tree

To sample a tree compatible with the partition, we need its full conditional distribution. By assuming the prior distributions in ((8)) and (9), it is not difficult to see that such a distribution is the uniform distribution over the subset of trees compatible with the current partition. Thus, at each step of the Gibbs sampler, it is sufficient to ensure that the new tree and current partition are compatible. Recall that compatibility is assumed when removing some edges from the tree produces the partition. To ensure that this constraint is satisfied, we consider the algorithm proposed by Teixeira et al. (2015). We first assign weights to the edges in the original graph. Edges that connect vertices belonging to the same group receive a low weight, whereas edges that connect vertices belonging to different groups receive a high weight. Specifically, we assume the Unif(0,1) distribution to generate low values and the Unif(10,20) distribution to generate higher values. Note that these values are arbitrarily assigned; the key is that the weights for edges connecting vertices from different groups must be higher than the weights of other edges. Once the weights are assigned, we use a minimum spanning tree (MST) algorithm to sample a tree that is compatible with the current partition.

In Computer Science literature, there are different algorithms designed to find a minimum spanning tree for a weighted undirected graph. The idea behind these algorithms is to compute the spanning tree with the minimal sum of weights. By using one MST algorithm and following the proposed weight assignments, edges connecting vertices in the same component will be selected before edges that connect vertices in distinct components, ensuring that the resulting spanning tree respects the current partition. In this case, we use the Prim algorithm (Jungnickel, 2013), which is preferred when there are a large number of edges in the graph.

## D Prior elicitation

As presented in the main manuscript, the values of  $\nu$  and  $\kappa$  have a significant impact on the number of clusters  $k$ . Expressions for the mean (18) and variance (19) can guide the setting of the hyperparameters  $\nu$  and  $\kappa$  according to the  $k$  that one expects to estimate. In the case of the dengue data used in Section 6 of the main manuscript, assuming  $\nu \approx 10$  and  $\kappa \approx 100$  implies  $k = 14$ , which represents approximately 10% of the total areas. Considering this, we explored three prior settings for  $\nu$  such that the mean is fixed,  $\mathbb{E}(\nu) = 10$ , while the variance varies with  $\mathbb{V}(\nu) = 10, 5, 1$ . To do so, we assumed Ga(10,1), Ga(20,2), and Ga(100,10), respectively. Similarly, we set three prior distributions for  $\kappa$  with  $\mathbb{E}(\kappa) = 100$  and  $\mathbb{V}(\kappa) = 100, 10, 1$ . In this case, we used Ga(100,1), Ga(1000,10), and Ga(10000,10), respectively. Figure 16 displays the posterior distributions of  $k$  over time under these prior distributions. In Figure 16(A), the prior distribution of  $\nu$  varies as mentioned, while  $\kappa$  follows a Ga(100,1) distribution. Conversely, Figure 16(B) presents a scenario where the prior distribution of  $\nu$  is Ga(10,1) and  $\kappa$  varies as previously described. Overall, the *a posteriori* number of clusters is robust to the *a priori* variability of the  $\nu$  and  $\kappa$  distributions.

Another strategy was also considered for exploring the hyperparameter settings. Instead of fixing the means of  $\nu$  and  $\kappa$  in order to estimate a certain number of clusters, we set prior distributions to estimate different values of  $k$ . Specifically, we set  $\nu$  and  $\kappa$  considering an *a priori* mean of  $\mathbb{E}(k) = 14, 29, 44$ , which

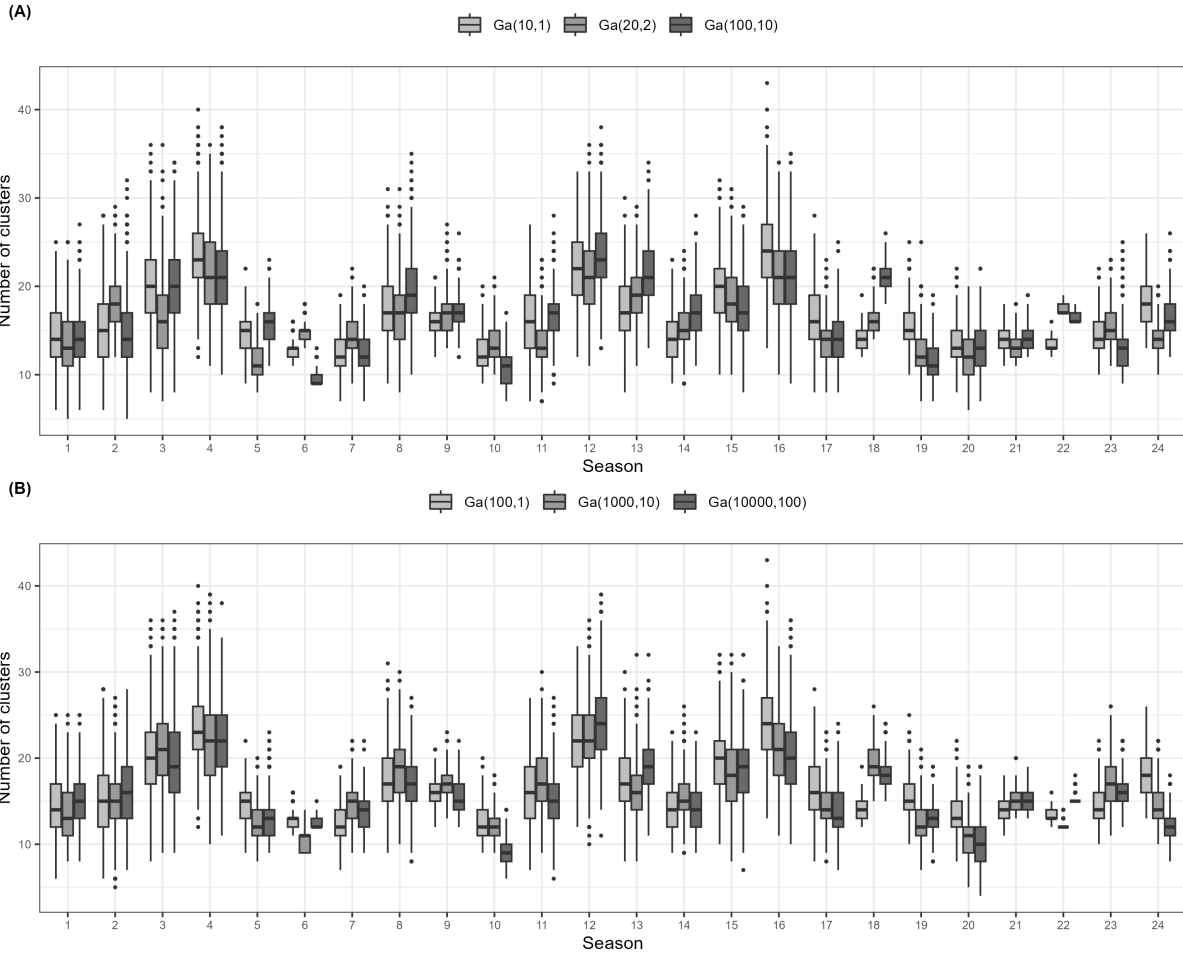


Figure 16: Posterior distributions of the number of clusters ( $k$ ) under different prior distributions for: (A)  $v$  and (B)  $\kappa$ . The results were obtained by fitting the model to the application data.

corresponds to 10%, 20%, and 30% of the total number of areas in the study. Figure 17 shows the posterior distributions of  $k$  under these settings. It can be seen that there was more variation in the posterior distributions of  $k$  than previously observed in Figure 16. This suggests that it is desirable to have an *a priori* understanding of the number of clusters one expects to estimate.

Another parameter that needs its distribution defined is  $\zeta$ . As seen in Section 4.2,  $\zeta$  is the hyperparameter of the latent variables  $\{c_s\}$  and directly impacts the probability of removing edges,  $\rho_s$ , as well as its autocorrelation function, as shown in Eq. (15) of the main manuscript. To understand the effect of  $\zeta$  on  $\rho$ , we explore three settings for the prior distribution of  $\zeta$ . Figure 18 presents the posterior distributions of the probability of removing edges under the different prior distributions for  $\zeta$ . In general, the probabilities are robust to the prior specification, with slight differences in the posterior of  $\rho_s$ .

## E MCMC algorithm

In this section, we describe the Metropolis-within-Gibbs sampler algorithm used to obtain posterior samples from the model presented in Section 4 of the main manuscript. Recall that  $i = 1, \dots, n$ ,  $t = 1, \dots, T$ , and  $s = 1, \dots, n_s$  represent area, epidemiological week, and season, respectively. Additionally, let  $\Omega = \{z, \beta, \theta, \delta, \mathcal{T}, \pi, \rho, u, c, w, \zeta, v, \kappa\}$  denote the complete parameter vector. The algorithm is then given as follows:

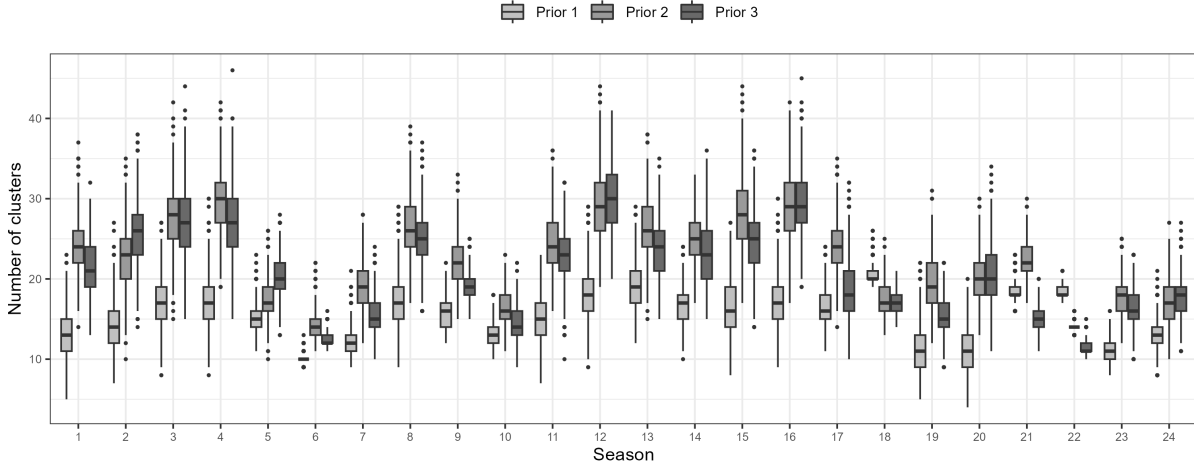


Figure 17: Posterior distributions of the number of clusters ( $k$ ) under different prior distributions for  $v$  and  $\kappa$ . The results were obtained by fitting the model to the application data.

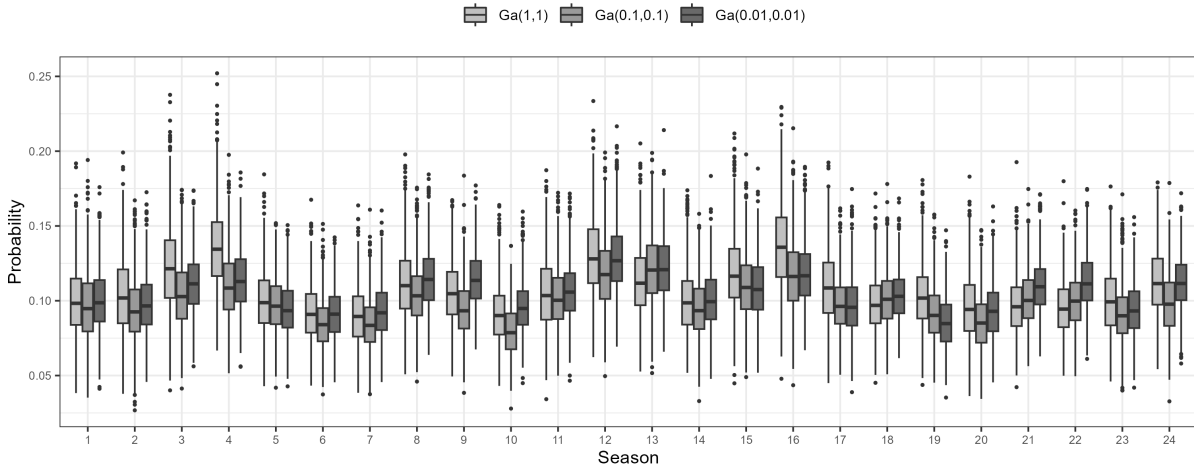


Figure 18: Posterior distributions of the probability of removing edges ( $\rho$ ) under different prior distributions for  $\zeta$ . The results were obtained by fitting the model to the application data.

1. Update  $v$ : the update of this parameter includes a random walk Metropolis–Hastings step, where the full conditional distribution is given by:

$$p(v \mid \cdot) \propto \left[ \prod_{s=1}^{n_s} \frac{\Gamma\left(v + \kappa + \sum_{l=0}^q c_{s-l}\right)}{\Gamma\left(v + \sum_{l=0}^q u_{s-l}\right)} \right] \frac{\Gamma(v + \kappa)}{\Gamma(v)} \left( w \prod_{s=1}^{n_s} \rho_s \right)^v v^{a_v - 1} \exp\{-b_v v\}.$$

2. Update  $\kappa$ : similar to the previous step, the update of this parameter also includes a random walk Metropolis–Hastings step, where the full conditional distribution is given by:

$$p(\kappa \mid \cdot) \propto \left[ \prod_{s=1}^{n_s} \frac{\Gamma\left(v + \kappa + \sum_{l=0}^q c_{s-l}\right)}{\Gamma\left(\kappa + \sum_{l=0}^q (c_{s-l} - u_{s-l})\right)} \right] \frac{\Gamma(v + \kappa)}{\Gamma(\kappa)} \left( (1 - w) \prod_{s=1}^{n_s} (1 - \rho_s) \right)^\kappa \kappa^{a_\kappa - 1} \exp\{-b_\kappa \kappa\}.$$

3. Update  $\zeta$ : the full conditional of this parameter is a well-known distribution, thus:

$$(\zeta \mid \cdot) \sim \text{Ga} \left( a_\zeta + \sum_{s=1}^{n_s} c_s, b_\zeta + n_s \right).$$

4. Update  $w$ : the full conditional for this parameter is also a widely recognized distribution, hence:

$$(w \mid \cdot) \sim \text{Be} \left( v + \sum_{s=1}^{n_s} u_s, \kappa + \sum_{s=1}^{n_s} (c_s - u_s) \right).$$

For  $s = 1, \dots, n_s$ , do:

5. Update  $\mathcal{T}_s$ : the following update is based on Prim's algorithm (Jungnickel, 2013). For each pair of edges belonging to the original graph, weights are assigned as follows:

- (a) the edges that connect vertices belonging to the same group receive a low weight,
- (b) the edges that connect vertices belonging to different groups receive a high weight.

Once the weights are assigned, the minimum spanning tree is obtained. This new sampled tree is compatible with the current partition.

6. Update  $\pi_s$ : as described in Section C.1, the sampling of a partition given a compatible spanning tree is performed based on Barry and Hartigan (1993)'s strategy of representing a partition as a vector of binary variables. Hence, let  $\mathbf{U}_s$  be the binary representation of the partition at season  $s$ , and  $l$  denotes the edge under evaluation.

For  $l = 1, \dots, n - 1$ , do:

6.1 Calculate

$$R_{ls} = \frac{\left( n - k_s + \kappa + \sum_{l=0}^q (c_{s-l} - u_{s-l}) - 1 \right) \Gamma(a)}{\left( k_s + v + \sum_{l=0}^q u_{s-l} - 1 \right) b^a} \frac{f^{(1)}(S_j)}{f^{(0)}(S_{j_1}) f^{(0)}(S_{j_2})},$$

$$\text{where } f_s(\mathbf{Y}_{S_j}) = \frac{\Gamma \left( a + \sum_{i \in S_j} \sum_{t \in s} y_{it} \right)}{\left( b + \sum_{i \in S_j} z_{is} \sum_{t \in s} E_{it} \exp\{\mathbf{X}_{it}^\top \boldsymbol{\beta}\} \right)^{\left( a + \sum_{i \in S_j} \sum_{t \in s} y_{it} \right)}}.$$

6.2 Sample:  $u \sim \text{Unif}(0, 1)$ .

6.3 Remove the edge if  $R_{ls} < \frac{u}{1-u}$ .

end of the loop iterating in  $l$ .

7. Update  $c_s$ : the update of this parameter includes a random walk Metropolis–Hastings step, where the full conditional distribution is given by:

$$p(c_s \mid \cdot) \propto \left[ \prod_{h=0}^q \frac{\Gamma \left( v + \kappa + \sum_{l=0}^q c_{s-l+h} \right)}{\Gamma \left( \kappa + \sum_{l=0}^q (c_{s-l+h} - u_{s-l+h}) \right)} \right] \frac{1}{(c_s - u_s)!} \left[ \zeta(1-w) \prod_{h=0}^q (1 - \rho_{s+h}) \right]^{c_s} \mathbf{1}_{[c_s \geq u_s]}.$$

8. Update  $u_s$ : similarly, the update of this parameter includes a random walk Metropolis-Hastings step, where the full conditional distribution is given by:

$$p(u_s | \cdot) \propto \left[ \prod_{h=0}^q \frac{1}{\Gamma\left(v + \sum_{l=0}^q u_{s-l+h}\right) \Gamma\left(\kappa + \sum_{l=0}^q (c_{s-l+h} - u_{s-l+h})\right)} \right] \binom{c_s}{u_s} \\ \times \left[ \frac{w}{(1-w)} \prod_{h=0}^q \frac{\rho_{s+h}}{(1-\rho_{s+h})} \right]^{u_s} \mathbb{1}_{[u_s \leq c_s]}.$$

9. Update  $\rho_s$ : the full conditional of this parameter is a well-known distribution, thus:

$$(\rho_s | \cdot) \sim \text{Be} \left( k_s + v + \sum_{l=0}^q u_{s-l} - 1, n - k_s + \kappa + \sum_{l=0}^q (c_{s-l} - u_{s-l}) \right)$$

10. Update  $\theta_s$ : this parameter is independently updated for each cluster, where its full conditional is a well-known distribution.

For  $j = 1, \dots, k_s$  do:

$$(\theta_{js}^* | \cdot) \sim \text{Ga} \left( a + \sum_{i \in \mathcal{S}_j} \sum_{t \in s} y_{it}, b + \sum_{i \in \mathcal{S}_j} z_{is} \sum_{t \in s} E_{it} \exp\{\mathbf{X}_{it}^\top \boldsymbol{\beta}\} \right)$$

end of the loop iterating in  $j$ .

11. Update  $z_s$ : This parameter is independently updated for each area, where its full conditional is a well-known distribution.

For  $i = 1, \dots, n$  do:

$$(z_{is} | \cdot) \sim \text{GIG} \left( \sum_{t \in s} y_{it} - \frac{1}{2}, 2\theta_{js}^* \sum_{t \in s} E_{it} \exp\{\mathbf{X}_{it}^\top \boldsymbol{\beta}\} + \exp\{\mathbf{V}_{is}^\top \boldsymbol{\delta}\}, \exp\{\mathbf{V}_{is}^\top \boldsymbol{\delta}\} \right)$$

end of the loop iterating in  $i$ .

end of the loop iterating in  $s$ .

Steps 12 to 16 are included to generate the  $q$  extra values of  $\mathbf{u}$ ,  $\mathbf{c}$ , and  $\boldsymbol{\rho}$  used in steps 7 and 8.

For  $s = n_s + 1, \dots, n_s + q$ , do:

12. Update  $\mathcal{T}_s$ : Repeat step 5.

13. Update  $\pi_s$ : analogous to step 6, let  $\mathbf{U}_s$  be the binary representation of the partition at season  $s$ , and  $l$  denotes the edge under evaluation. Then the prior distribution defined in Eq.(8) is used to obtain the ratio  $R_{ls}$

For  $l = 1, \dots, n - 1$ , do:

- 13.1 Calculate  $R_{l_s} = \frac{1-\rho_s}{\rho_s}$ .
- 13.2 Sample:  $u \sim \text{Unif}(0, 1)$ .
- 13.3 Remove the edge if  $R_{l_s} < \frac{u}{1-u}$ .

end of the loop iterating in  $l$ .

14. Update  $c_s$ : Repeat step 7.
15. Update  $u_s$ : Repeat step 8.
16. Update  $\rho_s$ : Repeat step 9.

end of the loop iterating in  $s$ .

17. Update  $\beta$ : the following update includes a random walk Metropoli-Hastings step, where the full conditional distribution is given by:

$$p(\beta \mid \cdot) \propto \exp \left\{ \sum_{i=1}^n \sum_{t=1}^T y_{it} \mathbf{X}_{it}^\top \beta \right\} \exp \left\{ - \sum_{s=1}^{n_s} \sum_{t \in s} \sum_{j=1}^{k_s} \sum_{i: c_i=j} E_{it} z_{is} \theta_{j_s}^* \exp \left\{ \mathbf{X}_{it}^\top \beta \right\} \right\} \\ \times \exp \left\{ - \frac{1}{2} (\beta - \boldsymbol{\mu}_\beta)^\top \boldsymbol{\Sigma}_\beta^{-1} (\beta - \boldsymbol{\mu}_\beta) \right\}.$$

18. Update  $\delta$ : similar to step 17, the update of this parameter includes a random walk Metropoli-Hastings step, where the full conditional distribution is given by:

$$p(\delta \mid \cdot) \propto \exp \left\{ \frac{1}{2} \sum_{i=1}^n \sum_{s=1}^{n_s} \mathbf{V}_{is}^\top \delta \right\} \exp \left\{ - \sum_{s=1}^{n_s} \sum_{t \in s} \sum_{i=1}^n \frac{\exp \left\{ \mathbf{V}_{is}^\top \delta \right\} (z_{is} - 1)^2}{2z_{is}} \right\} \\ \times \exp \left\{ - \frac{1}{2} (\delta - \boldsymbol{\mu}_\delta)^\top \boldsymbol{\Sigma}_\delta^{-1} (\delta - \boldsymbol{\mu}_\delta) \right\}.$$

## F Simulation study

In this section, we provide an in-depth explanation of two simulation studies that illustrate various aspects of the model we proposed. We chose the 70 microregions of the Brazilian state of Minas Gerais as our underlying map (i.e.,  $i = 1, \dots, 70$ ), where two regions are treated as neighbors if they share a common geographic boundary. To perform posterior inference, we saved samples of size 1,000 obtained after running 10,000 iterations, discarding the first 70% as burn-in, and thinning by 3 to avoid correlation. Convergence was monitored graphically. Models were fitted with the following prior specifications:  $\boldsymbol{\mu}_\beta = \boldsymbol{\mu}_\delta = \mathbf{0}$  and  $\boldsymbol{\Sigma}_\beta = \boldsymbol{\Sigma}_\delta = 10\mathbf{I}$ , allowing considerable variability for regression coefficients in both mean and dispersion components. We also assumed  $a_\theta = b_\theta = 1$ , so that the offset plays an important role in explaining the outcome. As mentioned before, the values of  $v$  and  $\kappa$  directly affect the number of clusters. Based on Table 1, we set  $a_v = 10$ ,  $b_v = 1$ ,  $a_\kappa = 100$ , and  $b_\kappa = 1$ , which implies an *a priori* expected number of clusters equal to 7, representing 10% of the total number of areas. Finally,  $\mathbf{c}$  is the parameter set affecting the temporal autocorrelation structure of  $\boldsymbol{\rho}$ . By defining  $a_c = 1$  and  $b_c = 1$ , we prevent  $\mathbf{c}$  from assuming very high values. Moreover, we are assuming that the *a priori* temporal correlation of the sequence of probabilities is low. We used the WAIC to check the goodness of fit. To evaluate the accuracy of partition estimates, we employed the method available in the `salso` R package (Dahl et al., 2020), using the VI loss function to estimate the partitions, and then we used the RI to measure the similarity between the true and estimated partitions.

## F.1 Simulation 1: comparing Poisson-inverse Gaussian and Poisson models

This first simulation study aims to compare the performance of spatio-temporal Poisson-inverse Gaussian and Poisson models when applied to equidispersed and overdispersed data. We assumed the model formulated in Section 4 of the main manuscript as a data-generating mechanism to create 100 synthetic datasets for each configuration. We created 156 time points representing the epidemiological weeks (i.e.,  $t = 1, \dots, 156$ ). Since a year consists of 52 weeks, this is equivalent to three years, leading us to 12 seasons, each lasting 13 weeks (i.e.,  $s = 1, \dots, 12$ ). To produce artificial scenarios that are faithful to reality, we used the observed information as offsets and covariates. The population size (per 100k people) of each area was considered as an offset, whereas temperature and humidity measured for each area and epidemiological week were taken as the covariates forming the design matrix  $\mathbf{X}$  (see Section 3 for the covariate descriptions). Regression coefficients were set to  $\boldsymbol{\beta} = (0.4, 0.1)$  for temperature and humidity, respectively. The same clustering structure was used to generate all datasets. This arrangement consists of three different scenarios: Scenario 1 consists of a partition formed by four clusters that remain constant over time. In Scenario 2, each season has a different partition that remains the same over the years (i.e., summer’s partition is the same for all years, autumn’s partition is the same for all years, and so on). In this case, the partitions are made up of four, three, two, and two clusters for summer, autumn, winter, and spring, respectively. Finally, we consider a more complex case, Scenario 3, where the partitions are different for each season and year, resulting in 12 different cluster formations with two to seven clusters. Figure 19 displays the maps showing each partition structure considered in this simulation study.

Cluster-specific parameters were set with a two-units difference between clusters as follows:

$$\begin{array}{l}
 \text{Scenario 1} \\
 \boldsymbol{\theta}_s^* = (1, 3, 5, 7) \quad \text{for } s = 1, \dots, 12 \\
 \\
 \text{Scenario 2} \\
 \boldsymbol{\theta}_s^* = \begin{cases} (1, 3, 5, 7) & \text{for } s = 1, 5, 9 \\ (3, 5, 7) & \text{for } s = 2, 6, 10 \\ (3, 5) & \text{for } s = 3, 7, 11 \\ (1, 3) & \text{for } s = 4, 8, 12 \end{cases} \\
 \\
 \text{Scenario 3} \\
 \boldsymbol{\theta}_s^* = \begin{cases} (1, 3, 5, 7, 9, 11) & \text{for } s = 6 \\ (1, 3, 5, 7, 9, 11) & \text{for } s = 10 \\ (1, 3, 5, 7, 9) & \text{for } s = 9 \\ (1, 3, 5, 7) & \text{for } s = 1, 2, 5, 7, 11 \\ (1, 3, 5) & \text{for } s = 4, 12 \\ (5, 7) & \text{for } s = 3 \\ (1, 3) & \text{for } s = 8 \end{cases}
 \end{array}$$

All settings defined so far are common for all simulated datasets. The difference in producing equidispersed and overdispersed data lies in how the component  $z_{is}$ , which accounts for data heterogeneity, is defined. To produce equidispersed data, it is sufficient to assume  $z_{is} = 1$ , for all  $i$  and  $s$ , thus, the mean and variance will be equal. In the other case,  $z_{is}$  is randomly generated from the inverse Gaussian density as presented in (2). We used information on temperature and humidity to build the design matrix  $\mathbf{V}$ . Unlike  $\mathbf{X}$ , when constructing  $\mathbf{V}$ , the measurements were averaged over all weeks in each season. Furthermore,  $\mathbf{V}$  includes a column of 1s for the intercept term. Regression coefficients were set to  $\boldsymbol{\delta} = (-0.3, 0.2, -0.4)$  for intercept, temperature, and humidity, respectively. We fit the PIG and Poisson models with  $q = 1$  to analyze the synthetic datasets using the MCMC algorithm described in Section E.

The first facet of the proposed model to be studied is its ability to recover regression coefficients. To do so, we computed 95% credible intervals and then the coverage rate. Results are provided in Table 2, where each entry is an average value over all 100 datasets. The coverage associated with  $\boldsymbol{\beta}$  is similar for all models. This result was already expected since the regression structure used to explain the average is the same for all datasets. In general, these values tend to decrease as the partition formation becomes more complex. Even so, note that the posterior distributions of these parameters are very concentrated, indicating high precision. In the case of the  $\boldsymbol{\delta}$  coefficients, we observed that when the PIG model is applied to overdispersed data, it is able to recover these parameters. However, when we fit the PIG model to data where the mean and variance are equal, the model tends to overestimate these coefficients, especially the intercept. Furthermore, standard deviation values are much higher. This occurs because when estimating high values for  $\boldsymbol{\delta}$ , we obtain high values for  $\boldsymbol{\psi}$ , which implies that  $\mathbb{V}(z_{is}) \rightarrow 0$ , causing  $z_{is}$  to be estimated as equal to 1. Indeed, the coverage associated with  $\boldsymbol{z}$  is very high (approximately 1 for all scenarios); that is, in cases where the data are equidispersed, the model correctly estimates  $z_{is} = 1$ , which is equivalent to a Poisson model.



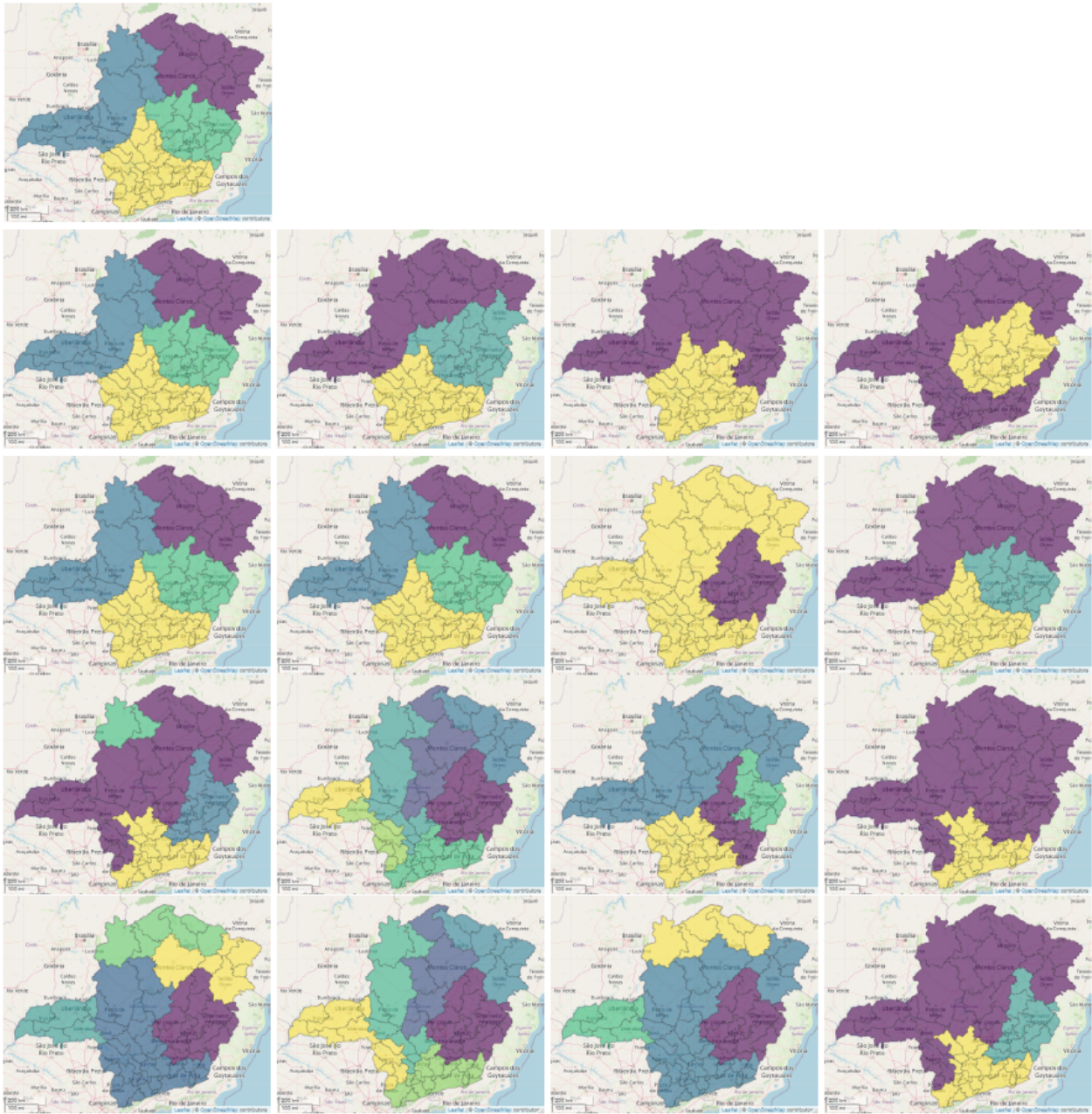


Figure 19: Map of spatial partitions used in Simulation 1. Row 1: Scenario 1 - a constant partition in time. Row 2: Scenario 2 - a different partition for each season that is repeated over the years. Rows 3-5: Scenario 3 - a different partition for each season and year.

For equidispersed data, the models demonstrate very similar performance, as shown in Table 2. In the case of overdispersed data, the PIG model proves to be advantageous, presenting lower values of WAIC, which is consistent across all scenarios. To evaluate the accuracy of partition estimates, we employed the method available in the `salso` R package (Dahl et al., 2020) with the VI loss function to estimate the 12 partitions for each synthetic dataset. To measure the similarity between the true and estimated partitions, we used the RI implemented in the same package. The higher the RI value, the closer two partitions are to each other.

Table 2 displays RI values averaged over 100 replicates and 12 seasons. Additionally, Table 3 presents RI values calculated for each time point. On average, the RI for the PIG and Poisson models when the data are equidispersed is approximately equal. In this case, the accuracy of the partition estimates obtained is high, which aligns with all previously mentioned findings. For overdispersed data, the Poisson model almost completely loses its clustering capacity, while the PIG model provides RI values exceeding 60% on average. The accuracy of partition estimation using the PIG model is further explored in Section F.2.

Table 2: Model fit performance metrics used to compare Poisson-inverse Gaussian and Poisson models applied to equidispersed and overdispersed data. Values are averaged over the 100 generated datasets. Coverage rate was calculated based on 95% credible intervals. Lower WAIC values indicate better fit. Higher RI value indicate higher accuracy of partition estimates.

Equidispersed		Coverage rate   posterior mean (standard deviation)								WAIC	RI		
		$\beta_1$	$\beta_2$	$\delta_0$	$\delta_1$	$\delta_2$							
Scce 1	PIG	0.98	0.40 (0.01)	0.99	0.10 (0.01)	0.00	9.51 (0.59)	0.83	-0.01 (0.57)	0.80	-0.36 (0.59)	53085	0.99
	Poisson	0.98	0.40 (0.01)	0.99	0.10 (0.01)	–	–	–	–	–	–	53086	0.99
Scce 2	PIG	0.97	0.40 (0.01)	0.68	0.11 (0.01)	0.00	9.62 (0.54)	0.83	0.13 (0.59)	0.65	-0.52 (0.57)	51416	0.96
	Poisson	0.98	0.40 (0.01)	0.68	0.11 (0.01)	–	–	–	–	–	–	51414	0.96
Scce 3	PIG	0.95	0.40 (0.01)	0.90	0.11 (0.01)	0.00	8.64 (0.52)	0.82	-0.04 (0.53)	0.85	-0.33 (0.56)	51373	0.98
	Poisson	0.98	0.40 (0.01)	0.87	0.11 (0.01)	–	–	–	–	–	–	51368	0.98
<b>Overdispersed</b>													
Scce 1	PIG	0.98	0.40 (0.00)	1.00	0.10 (0.00)	0.72	-0.16 (0.06)	0.96	0.13 (0.08)	0.82	-0.22 (0.09)	48756	0.65
	Poisson	0.98	0.40 (0.00)	1.00	0.10 (0.00)	–	–	–	–	–	–	49238	0.04
Scce 2	PIG	0.98	0.40 (0.00)	0.88	0.11 (0.00)	0.86	-0.19 (0.07)	0.96	0.13 (0.08)	0.92	-0.32 (0.09)	47182	0.61
	Poisson	1.00	0.40 (0.00)	0.84	0.11 (0.00)	–	–	–	–	–	–	47577	0.02
Scce 3	PIG	1.00	0.40 (0.00)	0.76	0.11 (0.00)	0.86	-0.21 (0.07)	0.98	0.16 (0.08)	0.94	-0.31 (0.09)	47108	0.65
	Poisson	0.98	0.40 (0.00)	0.60	0.11 (0.00)	–	–	–	–	–	–	47491	0.03

The conclusion drawn from this simulation study is that a PIG model can be applied to both equidispersed and overdispersed data. When overdispersion is not observed, the model assumes its particular case, which is equivalent to the Poisson model. Therefore, its ability to estimate and cluster is similar. However, the opposite does not occur. When a Poisson model is applied to overdispersed data, the model’s clustering capacity decreases drastically. In this case,  $\theta$  attempts to explain the interaction between the cluster-specific intercept and the dispersion parameter, making it difficult for areas to co-cluster.

## F.2 Simulation 2: exploring temporal dependence orders

We now turn our attention to the order of temporal dependence and its impact on clustering. In this case, we considered a clustering scenario where each season has a different partition that is repeated over the years. Following this structure, we examine two situations. In the first case, the number of clusters remains consistent, with 4, 3, 1, and 2 clusters for summer, autumn, winter, and spring, respectively. The second case presents greater variation in the number of clusters, with 5, 10, 4, and 2 clusters for the seasons. Figure 20 displays the maps showing each partition structure considered in this simulation study.

Table 3: Rand index over time. Values are averaged over the 100 generated datasets.

Equidispersed		RI											
		$s = 1$	$s = 2$	$s = 3$	$s = 4$	$s = 5$	$s = 6$	$s = 7$	$s = 8$	$s = 9$	$s = 10$	$s = 11$	$s = 12$
Sce 1	PIG	0.99	0.99	0.99	0.99	0.99	0.99	0.98	1.00	0.99	0.99	0.99	0.99
	Poisson	0.99	0.99	0.99	0.99	0.99	0.99	0.98	0.99	0.99	0.99	0.99	0.99
Sce 2	PIG	0.99	1.00	0.96	1.00	0.99	1.00	0.95	0.99	0.99	1.00	0.96	0.73
	Poisson	0.99	1.00	0.96	1.00	0.99	1.00	0.95	0.99	0.99	1.00	0.95	0.73
Sce 3	PIG	0.99	0.99	0.98	0.99	1.00	0.98	1.00	0.99	1.00	0.99	0.99	0.88
	Poisson	0.99	0.99	0.97	0.99	1.00	0.98	1.00	0.99	1.00	0.99	0.99	0.88
Overdispersed													
Sce 1	PIG	0.66	0.67	0.63	0.65	0.66	0.67	0.64	0.66	0.66	0.64	0.65	0.67
	Poisson	0.04	0.04	0.04	0.04	0.04	0.03	0.04	0.04	0.03	0.04	0.05	0.05
Sce 2	PIG	0.61	0.69	0.51	0.61	0.61	0.69	0.50	0.62	0.63	0.71	0.50	0.59
	Poisson	0.04	0.03	0.02	0.01	0.04	0.02	0.02	0.01	0.04	0.03	0.03	0.01
Sce 3	PIG	0.64	0.66	0.60	0.74	0.70	0.63	0.58	0.66	0.63	0.62	0.63	0.70
	Poisson	0.04	0.04	0.02	0.02	0.02	0.05	0.05	0.01	0.02	0.06	0.01	0.02

Table 4: 95% credible intervals for some model parameters. Values are averaged over the 100 generated datasets.

Equidispersed		$\rho$	$v$	$\kappa$	$w$	$\zeta$
Sce 1	PIG	(0.03, 0.10)	(4.59, 9.35)	(86.07, 125.41)	(0.03, 0.13)	(0.59, 7.99)
	Poisson	(0.03, 0.10)	(4.59, 9.39)	(86.31, 124.99)	(0.03, 0.13)	(0.65, 7.99)
Sce 2	PIG	(0.01, 0.08)	(3.30, 7.38)	(86.79, 126.20)	(0.02, 0.11)	(0.64, 7.60)
	Poisson	(0.01, 0.08)	(3.34, 7.42)	(86.75, 126.31)	(0.02, 0.11)	(0.61, 7.81)
Sce 3	PIG	(0.03, 0.11)	(4.79, 9.87)	(85.27, 123.97)	(0.03, 0.13)	(0.70, 8.33)
	Poisson	(0.03, 0.11)	(4.82, 9.91)	(85.02, 123.79)	(0.03, 0.13)	(0.66, 8.22)
Overdispersed						
Sce 1	PIG	(0.02, 0.10)	(3.84, 8.79)	(86.17, 125.31)	(0.02, 0.12)	(0.60, 7.69)
	Poisson	(0.54, 0.72)	(45.85, 74.08)	(34.64, 52.30)	(0.55, 0.73)	(3.52, 15.07)
Sce 2	PIG	(0.02, 0.10)	(3.46, 8.55)	(85.57, 124.54)	(0.02, 0.12)	(0.61, 8.01)
	Poisson	(0.54, 0.73)	(45.73, 74.16)	(34.07, 51.23)	(0.56, 0.74)	(3.55, 15.2)
Sce 3	PIG	(0.02, 0.11)	(4.22, 9.73)	(85.19, 123.99)	(0.02, 0.13)	(0.66, 8.07)
	Poisson	(0.56, 0.74)	(46.85, 74.94)	(33.50, 50.39)	(0.57, 0.75)	(3.65, 15.15)

The cluster-specific parameters were set as follows:

$$\begin{aligned}
 \theta_s^* &= \begin{cases} (1, 3, 6, 9) & \text{for } s = 1, 5, 9, 13, 17 \\ (1, 5, 9) & \text{for } s = 2, 6, 10, 14, 18 \\ 1 & \text{for } s = 3, 7, 11, 15, 19 \\ (1, 4) & \text{for } s = 4, 8, 12, 16, 20 \end{cases} & \theta_s^* &= \begin{cases} (1, 10, 25, 45) & \text{for } s = 1, 5, 9, 13, 17 \\ (1, 10, 25) & \text{for } s = 2, 6, 10, 14, 18 \\ 1 & \text{for } s = 3, 7, 11, 15, 19 \\ (1, 10) & \text{for } s = 4, 8, 12, 16, 20 \end{cases} \\
 \theta_s^* &= \begin{cases} (1, 3, 6, 9, 13) & \text{for } s = 1, 5, 9, 13, 17 \\ (1, 3, 6, 9, 12, 16, 20, 25, 30, 35) & \text{for } s = 2, 6, 10, 14, 18 \\ (1, 3, 6, 9) & \text{for } s = 3, 7, 11, 15, 19 \\ (1, 4) & \text{for } s = 4, 8, 12, 16, 20 \end{cases} & \theta_s^* &= \begin{cases} (1, 10, 25, 45, 70) & \text{for } s = 1, 5, 9, 13, 17 \\ (1, 9, 20, 35, 55, 75, 100, 120, 150, 180) & \text{for } s = 2, 6, 10, 14, 18 \\ (1, 10, 25, 40) & \text{for } s = 3, 7, 11, 15, 19 \\ (1, 15) & \text{for } s = 4, 8, 12, 16, 20 \end{cases}
 \end{aligned}$$

Scenarios 1 and 2 refer to the same partition structure (first case), but with different values for the cluster-specific parameters. The same occurs with scenarios 3 and 4 (second case). This configuration allows us to

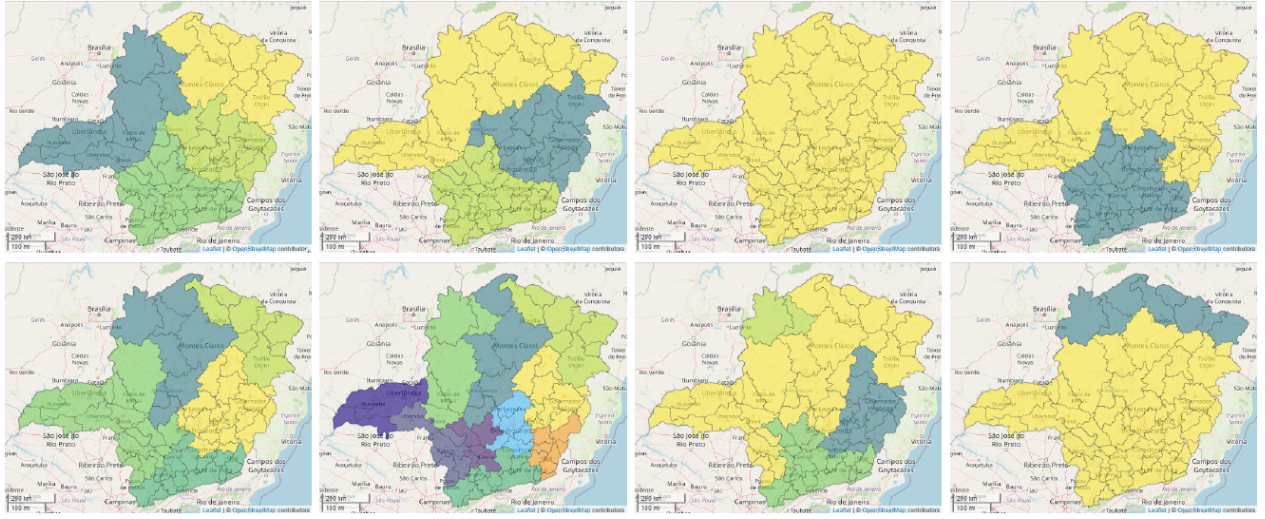


Figure 20: Map of spatial partitions used in simulation 2. Scenario where there is a different partition for each season that is repeated over the years. Row 1: partition used in scenarios 1 and 2. Row 2: partition used in scenarios 3 and 4.

compare the ability of the model to estimate the partition when the clusters are similar (scenarios 1 and 3), and when there are more pronounced differences among them (scenarios 2 and 4).

Once the partitions were created, the proposed model (Eq.(1)–(7) of the main manuscript) was considered as a data-generating mechanism to produce 100 synthetic datasets with 260 time points representing the epidemiological weeks (i.e.,  $t = 1, \dots, 260$ ). This is equivalent to 5 years, resulting in 20 seasons, each lasting 13 weeks (i.e.,  $s = 1, \dots, 20$ ). The design matrices  $\mathbf{X}$  and  $\mathbf{V}$ , as well as the regression coefficients  $\beta$ , were considered the same as in Section F.1. Meanwhile,  $\delta = (3.5, 0.2, -0.4)$ , which restricts the dispersion values to be around one. After generating the datasets, we fitted PIG models with  $q = 1, 2, \dots, 5$  to all synthetic datasets using the MCMC algorithm described in Section E. In addition, we fit a particular case where partitions were independently sampled. Note that to do this, it is sufficient to fix  $\mathbf{u} = \mathbf{c} = \mathbf{0}$ , thus  $\rho_s$  is independent and identically distributed as  $\text{Be}(v, \kappa)$ .

To evaluate the goodness of fit, we calculated the WAIC for each fitted model. Then, we computed the frequency with which each model obtained the lowest WAIC value over the 100 datasets, as displayed in Figure 21. Overall, adding a temporal structure to the partition prior tends to enhance the fit performance compared to using the independent version. The only case in which the model with independent partitions outperformed the others was scenario 3. However, it was unclear which dependency order yielded the best fit. Looking at the WAIC values averaged over the 100 generated datasets (Table 5), the differences between the models seem imperceptible. This occurred similarly in all four scenarios.

As shown in Figure 22 and Table 5, the model provided good accuracy in partition estimation, with RI values averaging over 90% across all scenarios. Nonetheless, similar to the WAIC, it is challenging to identify the best dependence order. On average, the RI values are comparable among the models (Figure 22). In fact, all parameters used in the temporal structure were estimated similarly among the models, as observed in Table 6.

## G Complementary results

In this section, we provide complementary results that support Section 6 of the main manuscript.

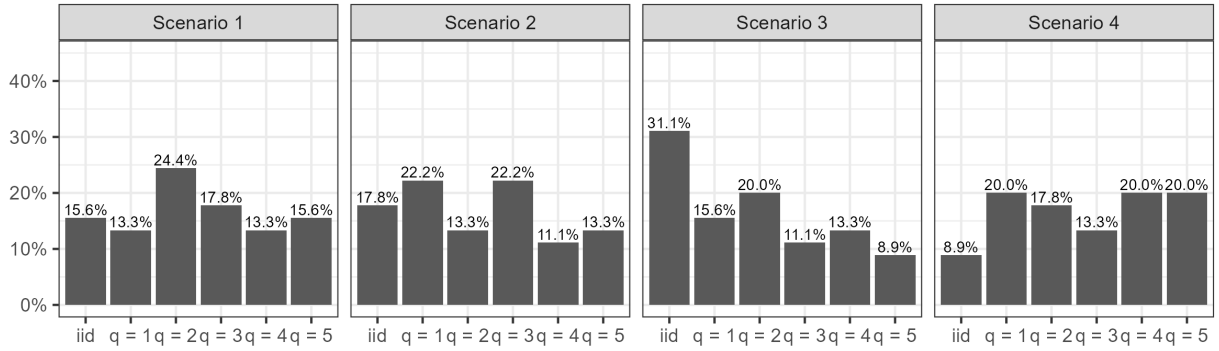


Figure 21: Barplot indicating how frequently each model obtained the lowest WAIC value over 100 datasets. In case of a tie, the simplest model was credited.

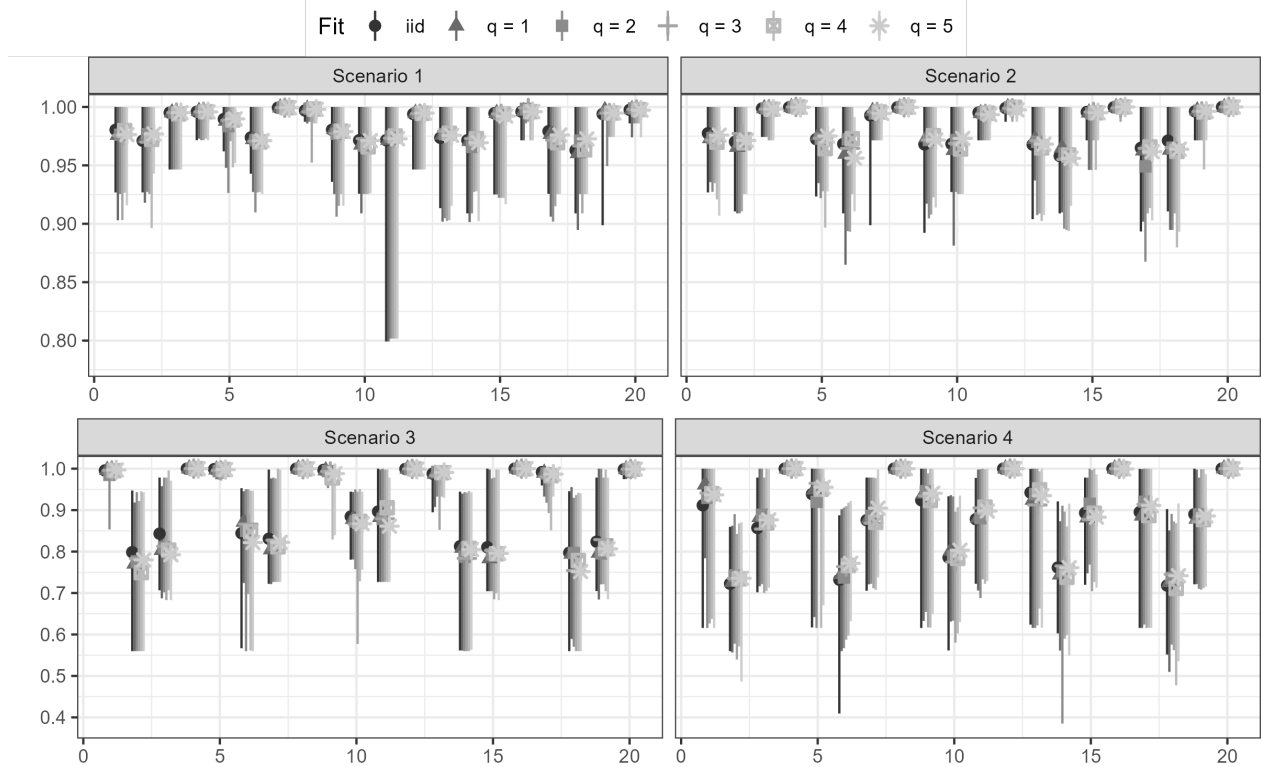


Figure 22: RI values to measure similarity between estimated and true partitions over time. Higher RI value indicate higher accuracy of partition estimates.

To address time-related trends in the dengue data, we analyzed a range of values for the dependence order parameter by adjusting  $q$  from 1 to 12, corresponding to three years. This approach allowed us to evaluate the impact of choosing  $q$  on the posterior inference of  $\rho$  and, in turn, on the partitioning. We also examined the simplest model where the partitions are treated as independent. Table 7 shows a posterior summary of the parameters related to temporal structure,  $\rho, v, \kappa, w,$  and  $\zeta$ , as well as the WAIC values used as a criterion for goodness-of-fit to determine the most suitable model. Regarding the estimated parameters,

Table 5: Model fit performance metrics used to compare different autoregressive order values. Values are averaged over the 100 generated datasets. Lower WAIC values indicate better fit. Higher RI value indicate higher accuracy of partition estimates.

		Fit							
		iid	$q = 1$	$q = 2$	$q = 3$	$q = 4$	$q = 5$		
Sce 1	WAIC   RI	77,078   0.98	77,079   0.98	77,077   0.98	77,078   0.98	77,078   0.98	77,077   0.98	77,077   0.98	77,077   0.98
Sce 2	WAIC   RI	87,055   0.98	87,051   0.98	87,054   0.98	87,052   0.98	87,055   0.98	87,055   0.98	87,053   0.98	87,053   0.98
Sce 3	WAIC   RI	87,497   0.92	87,505   0.91	87,504   0.91	87,505   0.91	87,506   0.91	87,506   0.91	87,504   0.90	87,504   0.90
Sce 4	WAIC   RI	104,672   0.89	104,668   0.89	104,670   0.89	104,671   0.89	104,668   0.89	104,668   0.89	104,669   0.90	104,669   0.90

Table 6: Summary for some model parameters. Values are averaged over the 100 generated datasets. Lower WAIC values indicate better fit.

Fit	95% credible intervals				
	$\rho$	$\nu$	$\kappa$	$w$	$\zeta$
iid	(0.01, 0.08)	(3.12, 6.39)	(88.07, 127.13)	–	–
$q = 1$	(0.01, 0.08)	(3.14, 6.57)	(87.90, 127.53)	(0.01, 0.08)	(2.27, 9.81)
$q = 2$	(0.01, 0.08)	(3.13, 6.59)	(87.66, 126.74)	(0.01, 0.08)	(2.35, 9.62)
$q = 3$	(0.01, 0.08)	(3.16, 6.70)	(87.32, 126.66)	(0.01, 0.08)	(2.30, 9.62)
$q = 4$	(0.01, 0.08)	(3.21, 6.80)	(87.13, 126.88)	(0.01, 0.07)	(2.33, 9.55)
$q = 5$	(0.01, 0.08)	(3.24, 6.98)	(87.11, 126.87)	(0.01, 0.07)	(2.40, 9.69)
iid	(0.01, 0.07)	(2.93, 6.12)	(87.90, 127.29)	–	–
$q = 1$	(0.01, 0.07)	(2.99, 6.22)	(87.95, 127.42)	(0.01, 0.08)	(2.33, 9.48)
$q = 2$	(0.01, 0.07)	(2.97, 6.29)	(87.41, 127.21)	(0.01, 0.07)	(2.26, 9.69)
$q = 3$	(0.01, 0.07)	(3.03, 6.42)	(87.25, 127.14)	(0.01, 0.07)	(2.18, 9.48)
$q = 4$	(0.01, 0.07)	(3.00, 6.45)	(87.03, 126.73)	(0.01, 0.07)	(2.29, 9.71)
$q = 5$	(0.01, 0.07)	(3.06, 6.53)	(86.95, 126.91)	(0.01, 0.07)	(2.36, 9.60)
iid	(0.03, 0.11)	(5.32, 9.79)	(85.63, 123.92)	–	–
$q = 1$	(0.03, 0.11)	(5.20, 9.76)	(85.39, 123.77)	(0.03, 0.12)	(2.49, 10.42)
$q = 2$	(0.03, 0.11)	(5.11, 9.75)	(85.55, 123.99)	(0.03, 0.12)	(2.38, 9.92)
$q = 3$	(0.03, 0.11)	(5.14, 9.89)	(85.63, 124.20)	(0.03, 0.11)	(2.43, 9.60)
$q = 4$	(0.03, 0.11)	(5.08, 9.84)	(85.18, 123.75)	(0.03, 0.11)	(2.32, 10.14)
$q = 5$	(0.03, 0.11)	(5.04, 9.94)	(85.40, 123.38)	(0.03, 0.11)	(2.47, 10.15)
iid	(0.03, 0.11)	(5.21, 9.56)	(85.95, 124.29)	–	–
$q = 1$	(0.03, 0.11)	(5.20, 9.74)	(85.86, 124.33)	(0.03, 0.12)	(2.41, 9.89)
$q = 2$	(0.03, 0.11)	(5.12, 9.70)	(85.88, 124.13)	(0.03, 0.11)	(2.51, 9.99)
$q = 3$	(0.03, 0.11)	(5.21, 9.91)	(85.69, 124.04)	(0.03, 0.11)	(2.40, 10.05)
$q = 4$	(0.03, 0.11)	(5.09, 9.84)	(85.98, 123.83)	(0.03, 0.11)	(2.41, 9.86)
$q = 5$	(0.03, 0.11)	(5.13, 10.06)	(85.21, 123.76)	(0.03, 0.11)	(2.56, 10.12)

we noticed a significant similarity among the results obtained from different temporal orders, particularly for the probabilities of removing edges. When evaluating the WAIC values, we observed that assuming a first-order autoregressive structure is the best option for fitting the dengue data from the Southeast region of Brazil. It is worth noting that the highest WAIC value was obtained in the case of independent partitions, which corroborates the need to consider temporal correlations between spatial partitions.

Results presented from now on were obtained by fitting the proposed model with a dependence order of

Table 7: Summary for some model parameters. Lower WAIC values indicate better fit.

Fit	95% credible intervals					WAIC
	$\rho$	$\nu$	$\kappa$	$w$	$\zeta$	
iid	(0.07, 0.18)	(10.64, 16.45)	(84.04, 117.55)	-	-	878,186
$q = 1$	(0.07, 0.18)	(9.73, 16.28)	(81.14, 117.73)	(0.08, 0.21)	(3.96, 15.49)	<b>814,474</b>
$q = 2$	(0.07, 0.18)	(8.66, 15.50)	(80.20, 117.83)	(0.08, 0.19)	(3.46, 13.05)	819,334
$q = 3$	(0.07, 0.19)	(8.68, 17.11)	(79.96, 117.60)	(0.08, 0.19)	(3.81, 12.03)	820,384
$q = 4$	(0.07, 0.17)	(8.86, 15.87)	(82.61, 118.51)	(0.08, 0.18)	(3.33, 11.05)	827,939
$q = 5$	(0.08, 0.19)	(9.29, 16.87)	(80.66, 116.92)	(0.09, 0.20)	(4.12, 13.69)	824,301
$q = 6$	(0.07, 0.17)	(8.47, 15.74)	(81.51, 119.62)	(0.08, 0.18)	(4.15, 13.52)	847,291
$q = 7$	(0.06, 0.16)	(7.70, 15.09)	(80.76, 118.52)	(0.07, 0.16)	(4.53, 13.94)	818,774
$q = 8$	(0.07, 0.17)	(8.15, 16.57)	(82.01, 119.02)	(0.08, 0.18)	(3.95, 15.83)	817,737
$q = 9$	(0.07, 0.18)	(9.13, 16.76)	(81.51, 118.52)	(0.08, 0.18)	(3.53, 12.29)	823,026
$q = 10$	(0.07, 0.17)	(7.93, 15.49)	(81.91, 118.09)	(0.08, 0.17)	(3.40, 12.03)	825,716
$q = 11$	(0.07, 0.17)	(8.06, 15.30)	(81.74, 118.20)	(0.08, 0.16)	(3.66, 14.52)	816,214
$q = 12$	(0.07, 0.17)	(8.04, 15.57)	(81.84, 120.34)	(0.08, 0.16)	(3.89, 12.30)	844,795

$q = 1$ , see Section 6 of the main manuscript for further details. Figure 23 illustrates the temporal dependence of the estimated partitions based on various measures, including lagged RI values, the posterior distribution of  $\{\rho_s\}$ , and the autocorrelation function of  $\{\rho_s\}$ . Figure 24 complements Figure 4 in the main manuscript by showing the geographic distribution of dispersion indicators for all seasons from 2018 to 2023. To complement Figure 5 in the main manuscript, we present the ratio  $\mathbb{E}(Y_{it} | \lambda_{it}, \psi_{is}) / \mathbb{V}(Y_{it} | \lambda_{it}, \psi_{is})$ , calculated over time for the capitals of each state. We observe that Belo Horizonte (MG), Rio de Janeiro (RJ), and São Paulo (SP) exhibited overdispersion throughout the entire period, as shown in Figures 25(A), (C), and (D), respectively. In contrast, Vitória (ES) demonstrated a period of equidispersion in mid-2021, as illustrated in Figure 25(B). A graphical representation of the product  $\mathbf{Oz}\boldsymbol{\lambda}$ , which indicates Poisson's rate, is shown in Figure 26. In this case, we calculated  $\mathbf{Oz}\boldsymbol{\lambda}$  for Januária (MG) and Campinas (SP) to complement the discussion presented in the main manuscript. Finally, Figure 27 illustrates the posterior distribution of the regression coefficients.

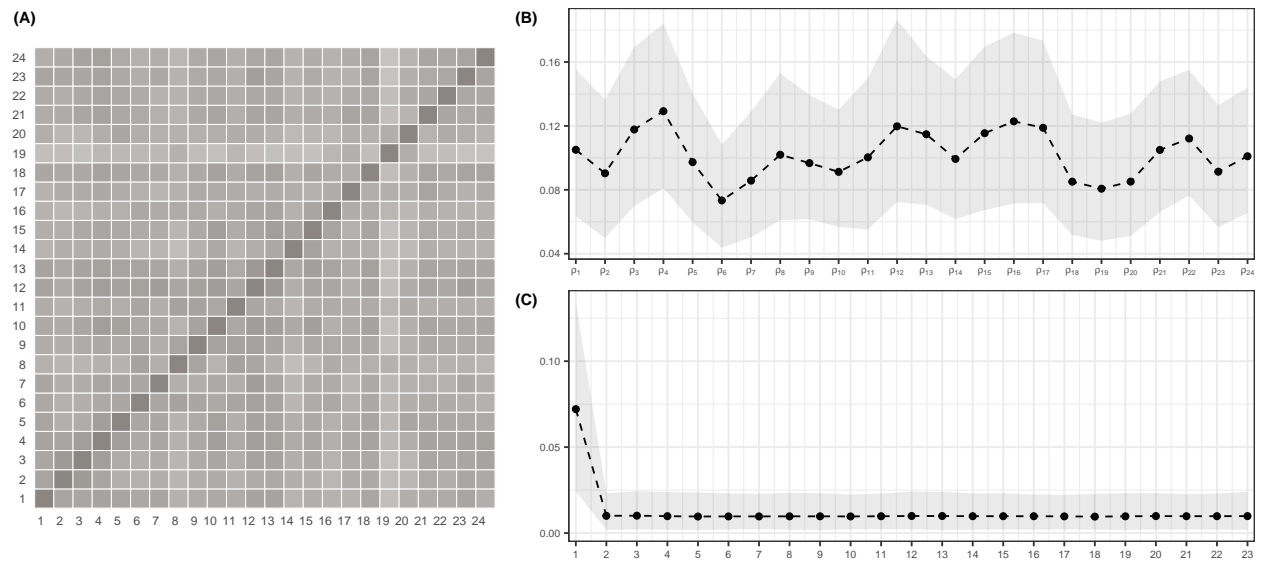


Figure 23: Temporal dependence of estimated partitions. (A) Summary of the lagged RI values. (B) Posterior mean and 95% credible interval of the probability of removing edges at each season  $\{\rho_s\}$ . (C) Autocorrelation function of  $\{\rho_s\}$ .



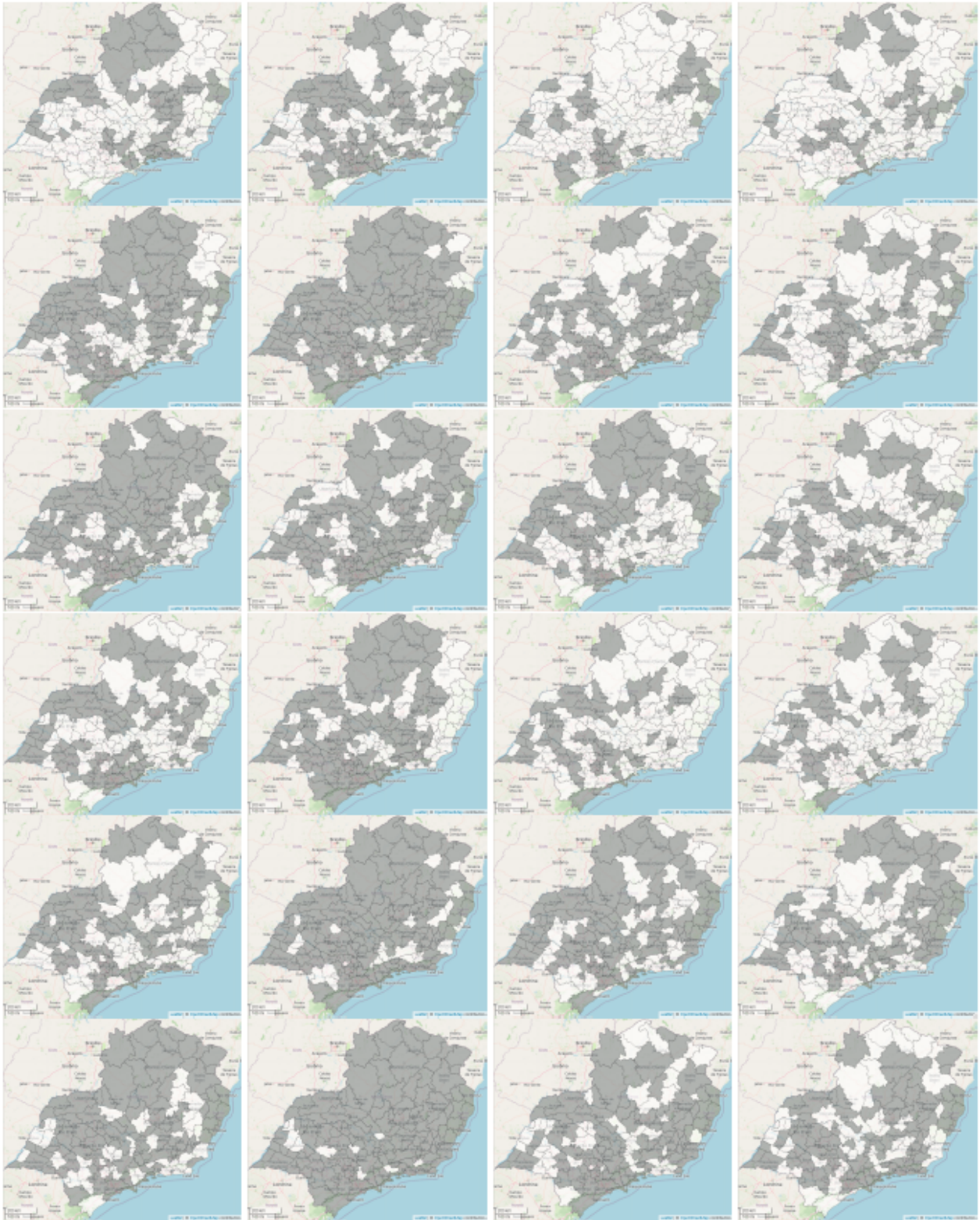


Figure 24: Dispersion indicators by areas constructed from the posterior distribution of  $z$  from 2018 (top) to 2023 (bottom) by seasons - summer (1st column), autumn (2nd column), winter (3rd column), and spring (4th column).  $z \approx 1$  (white);  $z \neq 1$  (gray).

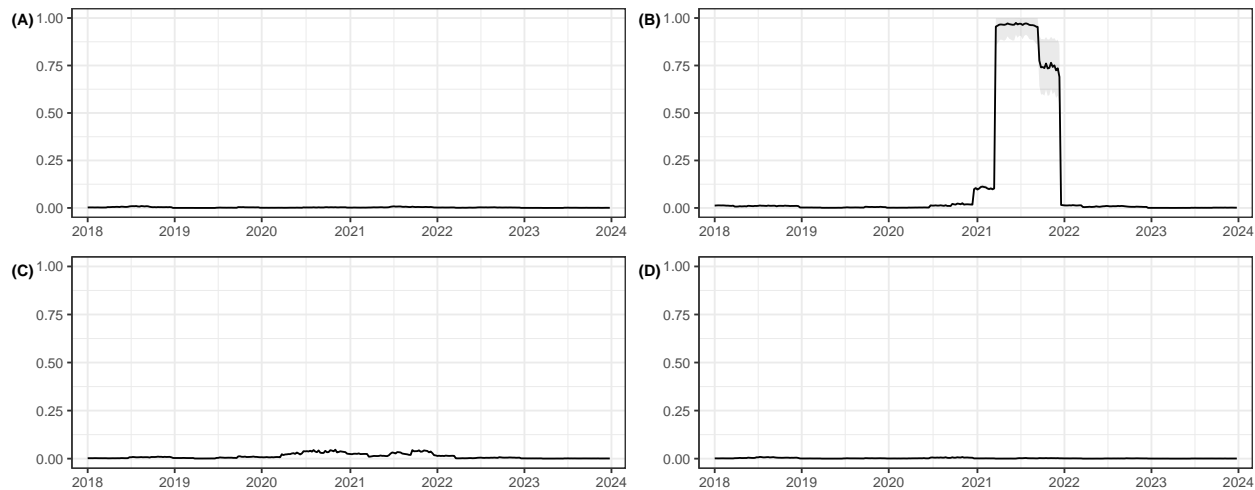


Figure 25:  $\mathbb{E}(Y_{it} | \lambda_{it}, \psi_{is}) / V(Y_{it} | \lambda_{it}, \psi_{is})$  over time for the capitals of each state. (A) Belo Horizonte - MG, (B) Vitória - ES, (C) Rio de Janeiro - RJ, and São Paulo - SP.

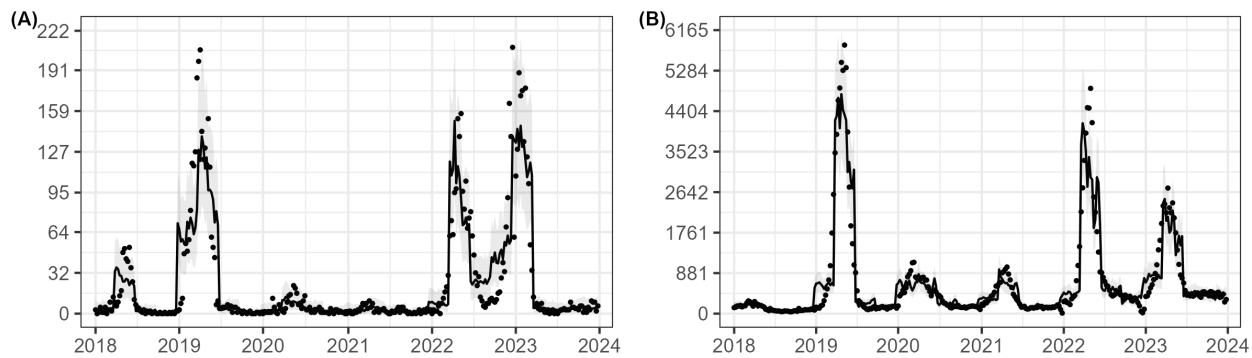


Figure 26: Observed number of cases (points) and estimated number of cases (solid lines) accompanied by its 95% credible intervals for two selected area. (A) Januária - MG and (B) Campinas - SP.

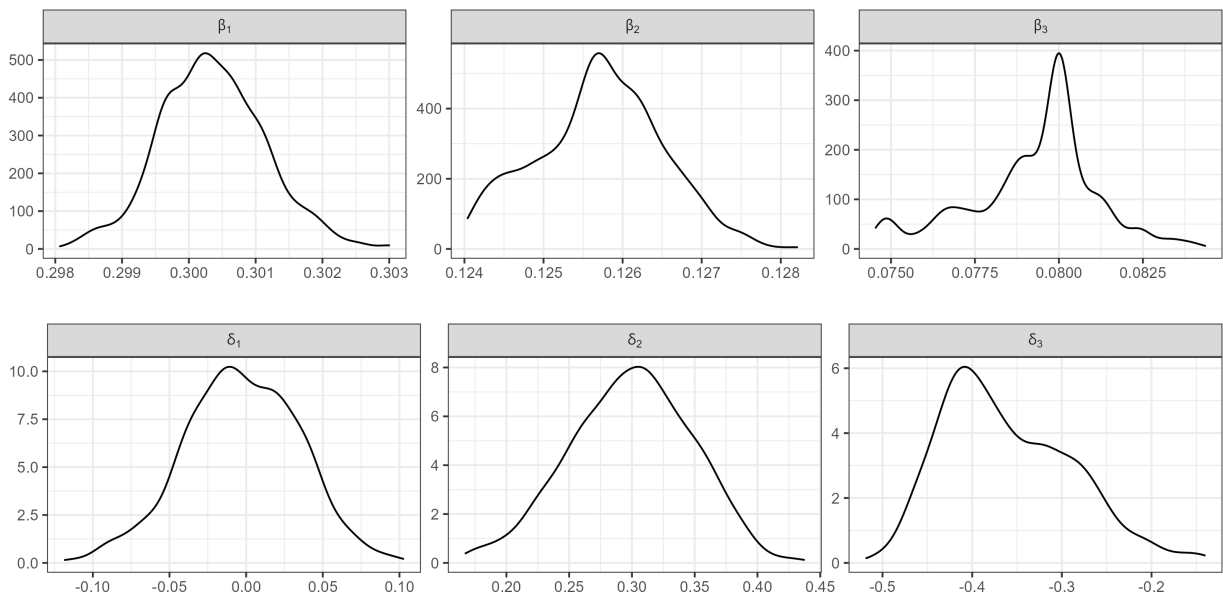


Figure 27: Posterior distribution of the regression coefficients. Used in mean struture:  $\beta_1$ ,  $\beta_2$ , and  $\beta_3$  corresponding to temperature, humidity, and HDI. Used in dispersion struture:  $\delta_0$ ,  $\delta_1$ , and  $\delta_2$  corresponding to intercept, temperature, and humidity.